



LUND UNIVERSITY
Faculty of Science

RBC deformability fractionation and hydrodynamic trapping for studying *Plasmodium Falciparum* infection

OSKAR STRÖM

Thesis submitted for the degree of Master of Science
Project Duration: 10 months

Supervised by
PROF. JONAS TEGENFELDT and STEFAN HOLM

Department of Physics
Division of Solid State Physics
January 2017

Contents

Abstract	iv
Acknowledgements	v
List of Abbreviations & Acronyms	vii
List of Figures	ix
1 Introduction	1
1.1 Thesis objectives	1
1.2 Microfluidics and Lab-on-a-Chip	1
1.3 Red Blood Cell Invasion by Malarial Parasites	2
1.4 Physical Changes Associated with Red Blood Cell Aging	2
1.5 Deformability-based Separation	2
1.6 Key Microfluidic Techniques	3
1.7 Thesis Outline	4
2 Microfluidic theory	5
2.1 The motion of fluids	5
2.2 The flow profile	6
2.3 Hydraulic resistance	7
2.4 Viscous drag	8
2.5 Viscous shear	8
2.6 Diffusion	10
3 Deterministic Lateral Displacement	11
3.1 Theory	11
3.2 Critical Size	12
3.3 Factors Influencing the Critical Size	12
3.4 The Effective Size of Particles	13
3.5 Deformability-based RBC Separation	14
4 Hydrodynamic Trapping	15
5 The Red Blood Cell	17
5.1 Mechanical properties of red blood cells	17
5.2 RBC-age Related Deformability changes	20
5.3 Dynamics of RBCs in fluid flow	21
6 <i>P. falciparum</i>	22
6.1 Invasion of Red Blood Cells	23
6.2 Characteristics of the Schizont and Merozoite stages	23

7	Materials and Methods	24
7.1	DLD Device	24
7.2	Device Design of Trapping Devices	24
7.3	Trap designs for parasite invasion on-chip	27
7.4	Numerical Simulation	29
7.5	Device Fabrication	30
7.6	Sample Preparation	32
7.7	Parasite Culturing	33
7.8	Experimental setup	33
7.9	Sterility	34
7.10	Data Analysis	35
8	Results and Discussion	37
8.1	Deterministic Lateral Displacement	37
8.2	Hydrodynamic Trapping	43
8.3	Parasite-infection on Chip	48
9	Conclusion	50
9.1	Outlook	50
	Appendix A: Sample extraction handling and preparation	52
	Appendix B: UV-lithography protocol	53
	Appendix C: Soft Lithography Protocol	55
	Appendix D: DLD array characteristics	56
	Bibliography	57

Copyright ©Oskar Ström 2016

Division of Solid State Physics
Department of Physics
Lund University
P.O Box 118
SE - 221 00 Lund
Sweden

Abstract

There have been several studies which indicate a preferential invasion towards younger red blood cells for the malarial parasite, *P. Falciparum*. Knowledge about a preferential mechanism could aid in the development of novel anti-malarial drugs. While the preference in these reports has been studied with density-separation of red blood cells (RBCs), separating the cells by deformability may be a more accurate method of isolating groups of RBCs with differing age. This thesis has investigated the details of separating RBCs by deformability in the microfluidic technique Deterministic Lateral Displacement (DLD). RBCs have been observed to undergo strong deformation in the device but the large size variation of RBCs together with RBC shape transformations inside the shallow channels have interfered with the separation by deformability. Further studies where higher device driving pressures with alternative device designs are utilized and the deformability of the separated cells are benchmarked towards existing techniques are proposed.

Furthermore, on-chip invasion of trapped RBCs has been investigated using hydrodynamic trapping arrays. The trapping arrays allow for convenient and highly-controllable investigation of the invasion dynamics. The trapping arrays have been fabricated using replica molding and been used to successfully immobilize RBCs. Trap occupancy rates up to 85% over the span of 14 min have been achieved. On-chip parasitic behavior has been investigated. It involved several complications including the prevention of late-stage parasite rupture due to shape transformation of RBCs into echinocytic (crenated cells) when introduced into shallow PDMS (polydimethylsiloxane) channels. This complication seem to affect the rupturing of late-stage infected RBCs inside the channels. Alternative materials and surface-coating should be explored to minimize any channel-derived artefacts.

Acknowledgements

I want to thank my supervisor prof. Jonas Tegenfeldt for the opportunity to work on such a stimulating project. I have much to thank my co-supervisor, Stefan Holm, for teaching me the inner intricacies of microfluidics. He has spent a lot of his time helping me in the cleanroom to fabricate devices and vizualizing structures with SEM.

A special thanks to Kushagr Punyani, that has been like a third supervisor during the project. His support and input into the project has been extremely valuable for me.

Thirdly, I am most grateful for Jason Beech who has generously shared his time and knowledge with me. He always gave me great feedback on my results.

I also want thank the rest of the Tegenfeldt Group: Trung, Bao and Rebekah for help and stimulating discussions during the process.

I want to thank Dr. Lisa C. Ranford-Cartwright & Laura Ciuffreda at University of Glasgow for a close collaboration and allowing me to come to work in the lab at Stockholm.

Last but not least, I would like to thank the master students I have been spending mostly of my time with for their encouragement and support. It was great fun in spite of all the late nights in the lab.

The work is funded by the People Programme in the project LAPASO (Marie Curie Actions) of the EU's FP7 under REA grant agreement n°607350.

List of Abbreviations & Acronyms

AFM	Atomic Force Microscopy
ATP	Adenosine Triphosphate
C	Viscosity contrast (Ratio of intracellular to extracellular fluid viscosity)
CAD	Computer-Aided Design
CPDA	Citrate Phosphate Dextrose Adenine
EDTA	Ethylened-Damine-Tetraacetic Acid
G	DLD gap distance
LOC	Lab-On-a-Chip
MAT	Micropipette Aspiration Technique
MCHC	Mean Corpuscular Hemoglobin Concentration
NO	Nitric Oxide
PDMS	Poly-Di-Methyl-Siloxane
<i>P. f</i>	<i>Plasmodium falciparum</i>
Pe	Peclét number
PLL-(g)-PEG	poly(l-lysine)-graft-Polyethyleneglycol
RBC	Red Blood Cell
RCF	Relative Centrifugal Force
Re	Reynolds number
R_c	Critical radius
R_{eff}	Effective radius in DLD
d_g	Trapping cup diameter
d_y	Trap array column distance
d_x	Trap array row distance
\mathbf{f}_b	Body forces
L_0	Characteristic length
\mathbf{u}	Velocity
U_0	Characteristic velocity
w	trap pore width
β	Width of first flow lane between posts in DLD
$\Delta\lambda$	DLD array row shift
γ	Shear strain
$\dot{\gamma}$	Shear strain rate

η	Dynamic viscosity
η_i	Internal cell viscosity
η_{2D}	2D cell membrane viscosity
η_{3D}	3D cell membrane bulk viscosity
θ	DLD displacement angle
θ	Trapping cup angle
λ	DLD row center-to-center distance
ρ	Density
τ	Shear stress

List of Figures

2.1.1 Schematics of flow at low (laminar) and high (turbulent) Reynolds number in a channel.	7
2.4.1 Illustration of the stokes drag of a spherical particle in laminar flow.	9
2.5.1 Illustration of couette flow	9
3.1.1 (a) Overview of the DLD parameters. (b) Illustration of the separate flow lanes in DLD.	12
3.2.1 Schematic of the separation process.	13
3.4.1 Schematics of a chirped DLD device	14
3.5.1 Separation by deformability in DLD	14
4.0.1 Illustration of the hydrodynamic trapping process	15
4.0.2 Single-cell trapping in a U-shaped structure	16
4.0.3 Single-cell trapping using u-shaped weir structures	16
5.1.1 Illustration of a normal red blood cell (discocyte).	19
5.1.2 Illustrative cross-sections of a concave stomatocyte, a biconcave discocyte and a spiculated echinocyte.	19
5.3.1 Two examples of RBC behavior in shear flow	21
6.0.1 Life cycle of <i>P. falciparum</i> in a human host	22
6.0.2 Morphology of <i>P. falciparum</i> merozoite (a) and schizont (b)	22
7.1.1 DLD device overview	25
7.2.1 3D illustration of RBC trapped in a simple single-trap design.	25
7.2.2 Trap array schematics	25
7.2.3 (a) Schematics of single trap variants with angle and pore width. (b) First generation trapping devices.	26
7.2.4 Hexagonal trap schematics	27
7.2.5 Schematic of the arc trap device	28
7.3.1 Schematics of trap design S5	29
7.5.1 An overview of the device fabrication process.	31
7.8.1 General experimental setup	34
7.10. Image analysis of outlet trajectories.	35
7.10. RBC geometry analysis	36
8.1.1 Simulation of shear rate and flow velocity in an DLD array	37
8.1.2 Deformation of RBCs in DLD	38
8.1.3 Various RBC morphologies in inlet area	38
8.1.4 DLD Outlet distributions	40
8.1.5 DLD Outlet distribution of a driving pressure of 500 mbar	41
8.1.6 Size distributions of the separated cells of outlet 1, outlet 3 from fig. 8.1.5 and a control sample.	41
8.1.7 RBC Deformation at 500 mbar	42
8.2.1 Trapping results of trap S3	43

8.2.2 Fabrication results of second generation devices	43
8.2.3 Scanning electron micrographs of trapping structures	44
8.2.4 Numerical flow velocity simulations around traps	45
8.2.5 RBC trapping	46
8.2.6 Array RBC trapping over time	46
8.2.7 Array RBC trapping over time	47
8.2.8 Simulation and trapping with the arc trap	47
8.2.9 Bead interaction to trapped cell	48
8.3.1 Micrographs from parasite-infection on chip experiments	49

Chapter 1

Introduction

1.1 Thesis objectives

The aim of this thesis project is to use the microfluidic separation technique, Deterministic Lateral Displacement (DLD), to fractionate the diverse population of red blood cells (RBCs) into subpopulations by their differing deformability. The objective is then for the subpopulations to be subject to invasion of malarial parasites to compare the respective invasion efficiency for the cells of each fraction. This could give insights into a potential age specific invasion preference as cell deformability is thought to increase with cell aging. Such an insight further the understanding of the malaria disease and could aid in the development of novel anti-malarial drugs.

In order to study malaria infections directly after fractionation in a convenient way inside the same microfluidic system, hydrodynamic cell trapping is utilized. The objective is to design and test various trap array designs for optimizing the trapping of RBCs with a following exposure to parasites.

Following is an introduction to subjects concerned in this thesis.

1.2 Microfluidics and Lab-on-a-Chip

Microfluidics is the science and technology of controlling and manipulating liquids at the micro-scale. Miniaturized fluidic systems can provide improved solutions for tasks and problems found in biology and medicine. Similar to how computers were able to go from filling whole rooms to smartphones, microfluidics hopes to turn the bulky labs of biotechnology and analytical chemistry into small and portable chips. The concept of fitting the function of entire laboratories on the surface of a silicon or polymer chip is the basis of Lab-on-a-chip (LOC) technology. There are many advantages to the miniaturization of fluidic systems. Smaller volumes mean smaller reagent consumption and potentially smaller power consumption. A drop of blood might be all that is necessary to diagnose a variety of blood-related diseases. Analysis can be made faster due to lower reaction times as molecules need to travel less distance. Having the entire system on a small portable chip allows for advanced technology in remote areas. The technology can be used in regions lacking the analytical and medical infrastructure and sophisticated laboratories that the developed world has access to. Disposable, point-of-care diagnostic devices, such as the pregnancy stick, can be used for more complex diseases providing instant diagnostic results. In its current infant state, microfluidic chips can be more expensive than competing solutions, but similar to the semiconductor industry, mass production would give rise to a significantly lower cost.

1.3 Red Blood Cell Invasion by Malarial Parasites

Malaria is a deadly disease (438 thousand deaths worldwide in 2015 [1]) caused by protozoan parasites transmitted into the human bloodstream via mosquitos. Inside the human host, the parasites eventually invade red blood cells. Inside the blood cells, where the parasites are hidden from the immune system, they proliferate until they finally burst out of the cells to continue the cycle. Certain malarial species, such as *Plasmodium vivax* and *Plasmodium ovale*, only invade RBCs of a certain age. *Plasmodium falciparum*, the deadliest variant of the malarial species, can invade RBC of all ages but it is unknown if an aged-based RBC invasion preference exists [2]. There are reports indicating that *P. falciparum* could have a preference towards invading younger RBCs [3] [4] but no conclusive evidence have been provided. A deeper understanding of the process giving rise to an age-based invasion preference could lead to the development of novel anti-malarial drugs.

1.4 Physical Changes Associated with Red Blood Cell Aging

Many cell properties have been reported to change with the aging of RBCs. Data from various studies indicate that physical changes include losses in cell volume and cell membrane surface area while there is an increase in the mean cellular hemoglobin concentration (MCHC) [5] [6].

The notion of a aging-coupled density increase is established among researchers. The use of density-separation to isolate the least and most dense cells are seen synonymously with isolating the youngest and oldest cell fractions [7] [8]. The *in vivo* density changes have been assumed to gradually increase over the RBC lifespan, where the very densest cells are thought to be the very oldest [7] [8]. In such studies, where the least and most dense cells are isolated, the densest cells have also been less deformable compared to the least dense cells [7] [8]. Combined rises of density and deformability have also been reported with studies observing in-vivo life span changes using biotin labels [5] [6]. In one of these studies, Franco et al. [6] challenge the view of progressive density increments. Rather, their data indicates that the density rise is concentrated in the early life of RBCs, making the use of density separation for old age RBC enrichment less effective, especially when trying to isolate the oldest cells. While the deformability rise could be similar to that of the proposed density changes, there are other factors determining the deformability than just the hemoglobin concentration which mainly dictates the cell density. As discussed in chapter 5, the membrane elasticity and bending rigidity are impaired with aging. As for the extreme age fractions, very young and very old cells, separating by deformability rather than by density could yield a better enrichment.

1.5 Deformability-based Separation

Various pathophysiological conditions, including malaria, sickle-cell anemia, diabetes mellitus and hereditary disorders can cause changes in RBC deformability [9] [10] [11] and this change in deformability can in turn cause further pathophysiological implications. This makes detecting differences in deformability for single cells clinically important

and likewise is physically separating differing cells important for being able to analyze deformability-coupled properties.

There exists a myriad of techniques capable of measuring the mechanical properties of RBCs but only a few that can separate RBCs based on the those properties. Techniques that can measure mechanical cell properties in bulk include the rotational viscometer [12] and ektacytometry [13]. These fail to take the cell population heterogeneity into account. Precise single-cell based techniques include nano-indentation by atomic force microscopy (AFM) [14], micropipette aspiration technique (MAT) [15], magnetic twisting cytometry [16], microplate deformation [17] and optical stretching [18]. The above mentioned techniques can make precise single-cell measurements but lack in throughput needed (less than 100 cells/h).

Microfluidic techniques capable of sorting by deformability include margination [19], inertial focusing [20], obstacles arrays [21]. None of these techniques can be used in high-resolution deformability studies for a large number of cells [22].

A new emerging microfluidic tool capable of high throughput and high-resolution is the microfluidic funnel ratchet. In it, oscillary flow is used to force cells through an array of increasingly narrower constrictions. Less deformable cells will not be able to pass through the narrowest paths and can then be separated from the more deformable cells. Guo et al. showed in 2016 how RBCs stiffened by the infection of *P. falciparum* could be enriched from blood with low parasitemia (blood parasite concentration) [23].

It is very difficult to completely disregard the effect of varying cell size when separating by deformability. However, if the deformability variation is significantly larger than that of the cell size, one can still study cell population based on deformability.

1.6 Key Microfluidic Techniques

The microfluidic separation method employed in this thesis is called Deterministic Lateral Displacement (DLD). It was first described by Huang et al. in 2004 [24]. There, they showed the possibility of using DLD to separate rigid spherical particles by size with a ultra-high resolution of ~ 10 nanometers.

DLD works by exploiting the distinct paths different particles take when colliding with pillars in a microchannel array. The array is designed so that particles with a radius smaller than a critical radius (R_c) move in the direction of the flow and particles with a radius larger than the R_c move in a direction dictated by the array. The array can then be split into sections of differing critical diameters to resolve a spectrum of particle sizes. This separation by steric interaction is simple without the need for external forces or biochemical labels which could otherwise make the process costly, time-consuming or overly complex.

Since Huang et al., the technique has been used to fractionate whole blood into its cellular components [25], isolate cancer cells from blood [26] and separating parasites (African trypanosomes) from blood [27] as a means for diagnosis.

In 2012, Beech et al. also showed the possibility to separate particles in DLD not only by size but also by shape and most relevant here, also by deformability [22]. While the involved dynamics are complex, the basic idea is that when the cells collide with the array posts they deform to different degrees and change their effective size accordingly. The

effective size of a particle, R_{eff} , is the radius of a hard spherical particle that would take an identical trajectory in the device. Holmes et al. later fractionated white blood cells by deformability [28] while others have simulated the use of deformability-DLD [29] [30] [31]. Most notably, Krüger et al. [30] simulated the separation of red blood cells based on their deformability in shallow microfluidic devices (channel depth of 4.8 μm).

Another microfluidic technique used in this thesis is called hydrodynamic trapping [32]. It is a passive method for trapping cells in microfluidic channels using cup-like structures. Just like DLD, it is extraordinarily simple as only the pressure supply driving the flow is needed. The technique utilizes the apparent high viscosity of water at the microscale. When a cell has flowed into a trapping cup, the streamlines that guided the cell into the trap instead help to keep the cell remain inside it. Several groups have scaled up the concept from single traps to large trapping arrays [33] [34]. The array-format can yield quantitative information on the single-cell level needed to statistically analyze the heterogeneous populations of biological cells.

Hydrodynamic trapping allows for a possibility to study single-cell processes at a high-quality using comparatively simple methods. Compared to other single-cell analysis methods like droplet microfluidics [35], static traps enable observation over time without the need for complicated droplet-tracking algorithms. With a trapping array, parasitic invasion dynamics can be studied in a highly-controlled and directly observable manner by using optical microscopy, without having to extract the cells for an external infection process.

1.7 Thesis Outline

To give an prerequisite understanding of the underlying microfluidic principles, chapter 2 gives an introduction to the fundamentals of microfluidic theory relevant to this thesis. Chapter chapter 4 and 3 goes into details of the two microfluidic techniques used; Hydrodynamic trapping and DLD respectively. The chapters deals with the core principles with theoretical explanation of the techniques.

Chapter 5 gives a fundamental overview of the red blood cell. The chapter focuses on its deformability and what factors influence it, including shape and cell aging.

Chapter 6 deals with the parasite *P. falciparum* and its invasion of RBcs.

The experimental methods and materials are presented in chapter 7. All the steps of the fabrication process of microfluidic devices are presented, and experimental procedures such as sample preparation and experimental setup is described.

Chapter 8 provides the experimental results together with following discussions. In the discussions, the results of fabrication, trapping and deformability-DLD are examined and interpreted with possible explanations.

Finally, chapter 9 gives concluding remarks and summarizes the thesis. An outlook for future improvements and experiments is included.

Chapter 2

Microfluidic theory

A fluid, either a gas or a liquid, is a material that continuously deforms under the pressure of a shear force. The fluids we encounter everyday are usually macroscopic and behave in a familiar and intuitive way. When scaling down a fluidic system to the micro-level, the fluids behave differently and to the unfamiliar eye, counter-intuitive. The effect of forces scales differently. Volumetric forces, such as gravity and inertia, have a smaller impact while surface forces such as surface tension and shear have a greater impact. The internal friction of fluids, viscosity, plays a larger role in microchannels. Just like the fluid friction in honey is greater than that in water, the internal friction of water confined to the microscale is higher than that of water on the macroscale. As a result, the liquid appears in unmixable stream lanes.

Understanding microfluidic theory is important for both deterministic lateral displacement and hydrodynamic trapping as their mechanism depends on the particular behavior of microscopic fluids. This chapters dives into the underlying theory of microfluidics.

2.1 The motion of fluids

The Navier-Stokes equation describes the motion of fluids. It is basically Newton's second law of mechanics ($\mathbf{F} = m\mathbf{a}$) applied to fluids. It describes the velocity, \mathbf{u} , and the pressure, p for a fluid with density, ρ , and dynamic viscosity η . The equation can be simplified by assuming the fluid to be Newtonian (stresses that arise from the flow are linearly proportional to the strain rate) which is the case for most fluids involved in microfluidics, see eq. (2.1.1) below:

$$\rho \left(\frac{\partial \mathbf{u}}{\partial t} + (\mathbf{u} \cdot \nabla) \mathbf{u} \right) = -\nabla P + \eta \nabla^2 \mathbf{u} + \mathbf{f}_b \quad (2.1.1)$$

$$\nabla \cdot \mathbf{u} = 0 \quad (2.1.2)$$

The left side of eq. (2.1.1) describes the changes in fluid momentum. The first term is due to changes in velocity over time for a given position (local acceleration) and the second term is due to changes in velocity when the fluid moves from one place to another (convective acceleration). The second term comes from the inertia of the fluid which produces history-dependant effects such as swirls or tornados.

The first term on the right describes the pressure gradient, the second describes the viscous effects, and the third expresses the body forces acting on the fluid, such as gravity or electrostatic forces.

In microfluidics, we can assume that the variations of pressure are so small compared to the speed of sound so that the ensuing density remain constant. The fluid can be treated as incompressible where the density is constant in time and space. This is expressed with the continuity equation, eq. (2.1.2).

As the second term of eq. (2.1.1), $(\mathbf{u} \cdot \nabla)\mathbf{u}$, is non-linear, Navier-Stokes is very difficult to solve analytically. In certain circumstances, such as in microfluidics, the equation can be substantially simplified. As will be shown later, convective acceleration is small and its term can be disregarded. There are usually no body forces acting on the fluid except for gravity, which itself is very small and can also be neglected. When assuming the fluid flowing in a straight channel with constant cross-section over the channel, the equation can be further simplified into:

$$0 = -\frac{\partial p}{\partial x} + \eta\left(\frac{\partial^2 u_x}{\partial y^2} + \frac{\partial^2 u_x}{\partial z^2}\right) \quad (2.1.3)$$

$$0 = \frac{\partial p}{\partial y} = \frac{\partial p}{\partial z} \quad (2.1.4)$$

To easily be able to discriminate whether a fluidic system is dominated by inertial or viscous forces, a dimensionless number called the Reynolds number, Re , is used. It is the ratio of the inertial term to the viscous term from the general Navier-stokes equation above, eq. (2.1.1):

$$Re = \frac{\text{inertial forces}}{\text{viscous forces}} = \frac{\rho L_0 U_0}{\eta} \quad (2.1.5)$$

where ρ is the fluid density, L_0 is the characteristic length of the system, U_0 is the characteristic fluid velocity, usually seen as the average flow velocity and η is the dynamic viscosity of the fluid (in this case water).

At a low Reynolds number which is characteristic for microfluidics, the viscous forces dominate the inertial. When the Reynolds number is very small ($\ll 1$), inertial forces become negligible and the flow becomes laminar, i.e. no turbulence or mixing of fluids. This implies that if the driving-forces behind fluid movement are removed, the fluid immediately stops. At a high Reynolds number, as in most of the everyday life, the inertial forces dominate, such as the turbulence observed when swirling a teaspoon around in a cup of coffee. The transition between these two modes depends on the surface roughness and the aspect ratio of the fluid confinement but is generally said to be around a Re of 800-2000.

The devices used in this thesis have a small Re ($\sim 1^{-2}$) and any inertial effects can therefore be disregarded.

2.2 The flow profile

The solution to eq. (2.1.3) and eq. (2.1.4) describes the velocity flow profile. The x component of the velocity \mathbf{u} will depend on the exact cross-sectional shape of the microchannel. To solve the previous equations, it is necessary to include boundary conditions. At the interface of a liquid and a solid, a “no-slip” boundary condition applies. It states that the velocity of the fluid at the walls must be zero; the fluid does not slip by the surface of the walls. It is the same phenomenon responsible for the thin layer of dust one can see on a blade of a blowing fan. The no-slip condition is why the dust closest to the wall doesn't

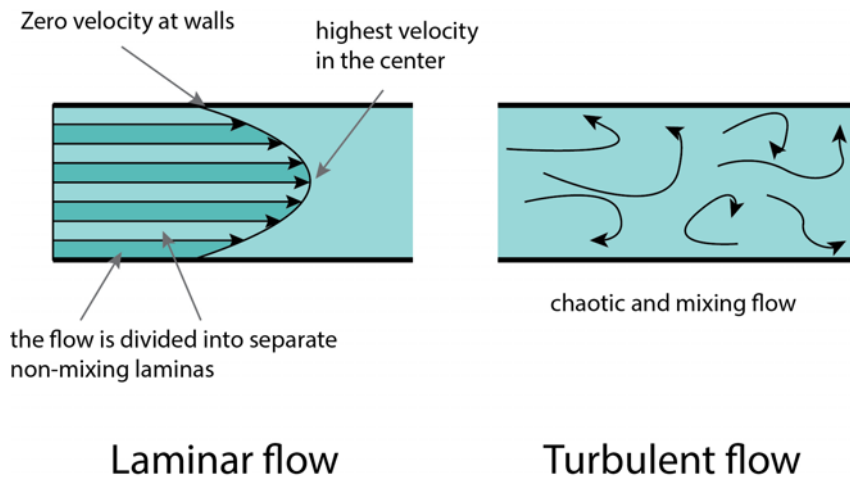


FIGURE 2.1.1: Schematics of flow at low (laminar) and high (turbulent) Reynolds number in a channel.

blow off when the fan moves at high speed.

As the flow velocity at the walls is zero, the flow profile takes the form of a parabola with the center mass moving at a faster rate, as seen in section 2.1. While many types of microchannel cross-section shapes are used in microfluidics, this thesis deals only with the rectangular shape. The parabolic flow will occur for both axes, resulting in a combined 3D-profile. However, if one axis is much larger than the other, the flow profile will become more plug-like.

2.3 Hydraulic resistance

Due to high surface-to-volume ratio in microchannels, the channel walls exert a lot of friction to the moving fluid. The channel is then said to have a high hydraulic resistance. This is contrasted to the macroscale where the inertia is high and the apparent friction is low. When the driving force responsible for the flow in a microchannel stops, the fluid immediately stops as a result of the friction. In a channel with a volumetric flow rate, Q , driven by a pressure difference, ΔP , the hydraulic resistance R_h can be calculated from the Hagen-Poiseuille law:

$$\Delta P = \frac{R_h}{Q} \quad (2.3.1)$$

Eq. 2.3.1 is analogous to Ohm's law where the electrical resistance is described by $\Delta U/I$. The hydraulic resistance for a rectangular cross-section with height h and width w containing a fluid with dynamic viscosity η is given by [36]:

$$\begin{aligned}
 R_h &= \frac{3\eta L}{4wh^3} \left[1 - \frac{192}{\pi^5} \frac{h}{w} \sum_{n=1,3,5,\dots}^{\infty} \frac{1}{n^5} \tanh\left(\frac{n\pi w}{2h}\right) \right]^{-1} \\
 &\approx \frac{3\eta L}{4wh^3} \frac{1}{1 - 0.63h/w}
 \end{aligned} \quad (2.3.2)$$

With a flat and wide channel, eq. (2.3.2) can with a very small error margin (0.2% for $h = w/2$ [37]) be approximated to [37]:

$$R_h = \frac{12\eta L}{1 - 0.64(h/w)} \frac{1}{h^3 w} \quad (2.3.3)$$

To continue the comparison with electronics, the resistance in straight channels in parallel and in series is analogous to the electrical resistance relationships in Kirchhoff's circuit laws. For series coupling of two channels with hydraulic resistances R_1 and R_2 the additive law applies:

$$R = R_1 + R_2 \quad (2.3.4)$$

For parallel coupling of two channels with hydraulic resistances R_1 and R_2 the inverse-additive law applies:

$$\frac{1}{R} = \frac{1}{R_1} + \frac{1}{R_2} \quad (2.3.5)$$

These two laws are only valid for flow at low Reynolds numbers and for long narrow channels.

As completely straight side-walls are difficult to fabricate, the cross-section is not completely rectangular. Together with variations in surface roughness, the hydraulic resistance equations can only be approximate for experimental flow experiments.

2.4 Viscous drag

When a particle, such as a biological cell, is flowing in a channel at low Reynolds number it experiences a fluid resistance in the direction of the flow. This viscous drag force is expressed by Stoke's law:

$$\mathbf{F}_{drag} = 6\pi\eta r\mathbf{u} \quad (2.4.1)$$

The law assumes a spherical, materially homogenous, smooth particle with radius r flowing with a velocity \mathbf{u} in a surrounding medium with a dynamic viscosity η . Eq. 2.4.1 is derived from Navier-stokes equation for low Reynolds number (eq. (2.1.1)).

If no other force is applied to the particle, it will continue flowing in its streamline. Other forces that can act on the particle include electrical, magnetic, thermal and steric. Electrical or magnetic forces is not of concern in this work. Thermal forces are omnipresent and discussed in the next section. The use of steric forces, caused by other solid structures acting on the particle, is central to DLD and hydrodynamic trapping. Next chapters will discuss the concept in detail.

2.5 Viscous shear

When an object is subject to a mechanical stress (force per unit area) it deforms. Strain is the measure of that deformation. A stress can either be normal (compression or tension)

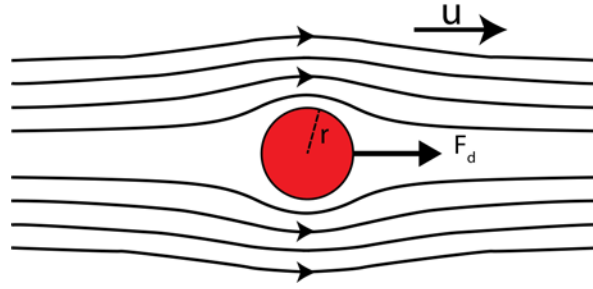


FIGURE 2.4.1: Illustration of the Stokes drag of a spherical particle in laminar flow.

or shear. Normal stress is perpendicular to the surface of the object:

$$\sigma = E\epsilon \quad (2.5.1)$$

where ϵ is the resulting strain and E is the elastic modulus or Young's modulus. Shear stress, τ , is parallel to the object surface and is described by:

$$\tau = G\gamma \quad (2.5.2)$$

where γ is the resulting shear strain and G is the shear modulus given by $G = \frac{E}{2(1+\nu)}$, where ν is the object's Poisson ratio.

For an isotropic and incompressible Newtonian fluid, the shear stress at a surface element at point y is defined as:

$$\tau = \eta\dot{\gamma} = \eta \frac{\partial u}{\partial y} \quad (2.5.3)$$

where η is the dynamic viscosity and $\dot{\gamma}$ is the shear strain rate, equal to the derivative of the flow rate perpendicular to the average flow direction u_x . At $y=0$, τ is greatest due to the no-slip condition, making the derivative of u_x highest. Eq. 2.5.1 depict the viscous shear created in a fluid between two parallel plates moving relative to each other.

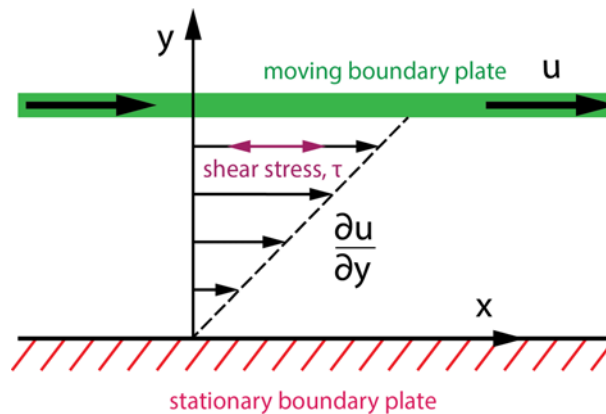


FIGURE 2.5.1: Illustration of Couette flow, the laminar flow of a viscous fluid between two infinitely wide parallel plates moving relative to each other.

2.6 Diffusion

The particle movement due to Brownian motion becomes important to consider in microfluidics. In some cases, it is utilized in the mixing of solutes which is otherwise difficult due to the mixing-resistance present in laminar flow. In DLD, the separation is compromised if particles diffuse across the streamlines between the array posts. While some diffusion is unavoidable, minimum diffusion is preferable as it has been shown to reduce the separation resolution [38] [39]. Particle diffusion is also significant for cell trapping. If the trapped cells diffuse out of the traps over time, the trapping will be ineffective.

The mean square displacement a particle diffuses is given by:

$$\langle x_n \rangle^2 = 2nDt \quad (2.6.1)$$

where n denotes the number of dimensions. The distance diffused depends the particle diffusion coefficient, D , and time duration, t .

The diffusion coefficient, D , is described by the Stokes-Einstein relation:

$$D = \frac{k_B T}{6\pi\eta r} \quad (2.6.2)$$

where D is determined by Boltzmann's constant, k_B , the temperature, T , and the dynamic viscosity of the solution, η .

In microfluidic devices, the distance travelled by diffusion depends on the residence time a particle has in the system. The dimensionless number, Pe , the Péclet number, describes the relative impact of advection (bulk fluid flow) to that of diffusion in terms of transportation, defined below:

$$Pe = \frac{\text{advective transport rate}}{\text{diffusive transport rate}} = \frac{uL_0}{D} \quad (2.6.3)$$

where u is the average flow velocity, L_0 is the characteristic length over where the competition between advection and diffusion takes place and D is the diffusion coefficient.

At high Péclet numbers, advection happen much faster than diffusion and thus the system is dominated by advection. Particles follow the streamlines of the flow and both DLD and the trapping mechanisms work efficiently. At low Péclet number, the opposite is true where the diffusion time is lower and particles can readily diffuse across streamlines.

In the experiments presented here, blood has been used as sample. A serum protein in blood has a radius of ~ 5 nm diffuses about $9 \mu\text{m}$ over the span of a second in one dimension. Compare that to a particle with a radius of about $3.8 \mu\text{m}$, like the red blood cell, that diffuses 300 nm for the same duration. The impact of diffusion increases with small flow velocities or long devices. After the duration of 1 minute, the RBC has an average 1D diffusion displacement of about $3 \mu\text{m}$.

Chapter 3

Deterministic Lateral Displacement

Deterministic Lateral Displacement (DLD) is a particle separation technique. The separation occurs inside a large array of pillars. When particles flow into the array, they are separated or not based on if the given particles fit inside a stream or not. The particles collide with the pillars which sterically force large particles to cross streamlines whereas smaller particles can stay in their existing flow lane. The lanes takes different trajectories and thus, the particles are separated in space. DLD separates particles continuously in a microfluidic array into physically separate reservoirs. It works in a passive way, without relying on forces other than the pressure driven flow. As its name suggests, the separation mechanism is deterministic, meaning that the path of a given particle is not based on stochastic processes like diffusion. Rather, the path is determined by the relationship of critical size of the device and the effective size of the particle. As described in the previous chapter, some diffusion still occurs over the length of the device, limiting the separation resolution.

For subsequent analysis of the separated fractions, a high throughput is desired. While DLD has been shown to separate cancer cells from whole blood at flow rates up to several ml/min [40], the shallow device ($\sim 4 \mu\text{m}$) used in this thesis increases the hydraulic resistance which reduces the flow rate and thus, limits the throughput. This shallow depth is however necessary to confine the disk-shaped RBCs to flow parallel to the floor of the channel for maximum deformation to take place.

This chapter describes the principle of DLD with special focus on deformability-based separation.

3.1 Theory

In DLD, the fluid flows past an array of micropillars, splitting into individual streamlines when crossing between the pillars. These pillars have a center-to-center distance denoted λ , and every row in the array is shifted a distance $\Delta\lambda$ as illustrated in fig. 3.1.1 a. The period of the array row shift, denoted N , is defined as:

$$N = \frac{\lambda}{\Delta\lambda} \quad (3.1.1)$$

Displacing particles are displaced in an displacement angle, θ , given by $\tan(\theta) = \frac{\Delta\lambda}{\lambda}$. The flow lanes shift cyclically, meaning that after N rows, the lanes will return to their initial positions. N thereby determines the number of flow lanes between the posts. In fig. 3.1.1 b, the cyclic behavior of the flow lanes is visualized with stall lines separating the lanes. Flow lane 1 moves to position 3 in the next row, then position 2 in the row after that, and finally returns to position 1. Between the posts, the flow lanes have to cross a narrower path so that they are compressed. Particles with a radius larger than

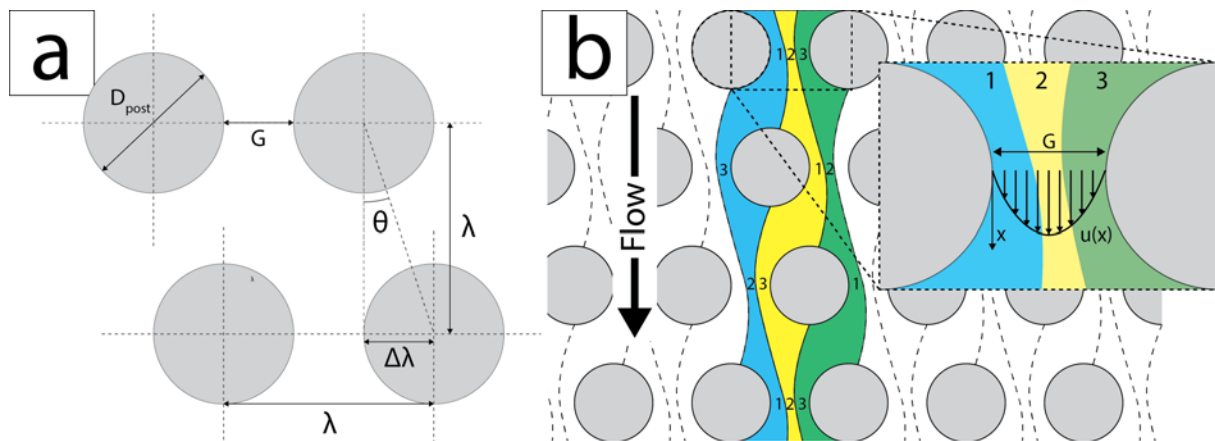


FIGURE 3.1.1: (a) Overview of the DLD parameters. (b) Illustration of the separate flow lanes in DLD. The zoomed-in window depicts an overlay of the parabolic flow profile onto the flow lanes

the width of the first flow lane are forced into the second flow lane. The larger particle will be bumped at every post, laterally displaced a distance $\Delta\lambda$ between every row. This behavior is called “displacement” or “bump” mode. Particles with a radius smaller than β will stay in the cyclic progression of the streamline, zig-zagging between posts without any long-lasting lateral movement. This behavior is called “zig-zag” mode. Figure 3.2.1 illustrates the two transit modes of DLD.

3.2 Critical Size

Thus, the path a particle will take depends if it is larger or smaller than a critical size, the width of the first streamline, β .

Davis [41] empirically derived a formula describing the critical size assuming a parabolic flow profile and separating rigid spheres:

$$R_c = \beta = \frac{1.4GN^{-0.48}}{2} \quad (3.2.1)$$

Fig. 3.2.1 shows how two particles with differing effective size, R_{eff} , result in separate trajectories depending on their relationship with R_c .

By combining sections of different critical size, one can separate multiple particles in the same DLD array. In fig. 3.5.1, the principle of a chirped array is illustrated.

3.3 Factors Influencing the Critical Size

Decreasing the post diameter relative to the the period and the gap will make the flow profile more plug-like with a reduced R_c . Vice-versa will lead to a stronger parabola. Decreasing the device depth relative to G and D_{post} also leads to a more plug-like flow with reduced R_c . Critical changes are not seen until below 3 μm of depth. [42]

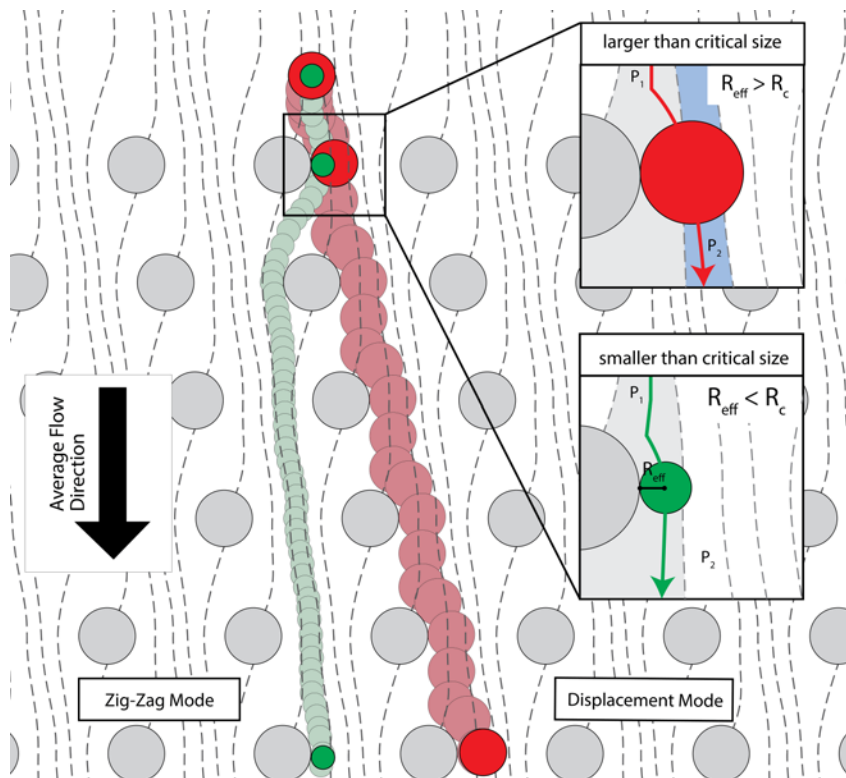


FIGURE 3.2.1: Schematic of the separation process.

3.4 The Effective Size of Particles

The particle parameter, R_{eff} , which determines whether displacement into the second streamline occurs, varies with the geometrical array design, the channel medium and the intrinsic properties of the particle. In the original DLD paper [24], hard spherical particles were used to show the principle of the technique. Due to the simplicity these particles bring, the separation can be described with a single parameter, R_c . The sizes or trajectories of rigid spheres are not altered by the shear flow. They also do not exhibit irregular motion as asymmetrical particles would.

The situation is different for biological particles. Cells are diverse in both shape and mechanical properties. Morphology can vary significantly even in a cell-population of the same cell type. The behavior of soft and non-spherical particles such as red blood cells in DLD is less understood which depends upon a complicated addition of a number of various factors [43]. These include the mechanical properties of the particles, particle-post and particle-particle interactions and the shear rate and velocity profile between the posts [42]. Also, when the particle shape is asymmetrical, the effective size varies on the particle orientation in the channel. Beech et al. [22] showed how varying the microchannel depth can confine particles into a certain orientation. By reducing the microchannel thickness, asymmetric particles, like RBCs, have to accommodate by laying down on their wide side, resulting in an increase in the effective size. This confinement also limits RBC tumbling motion which simplifies the dynamics.

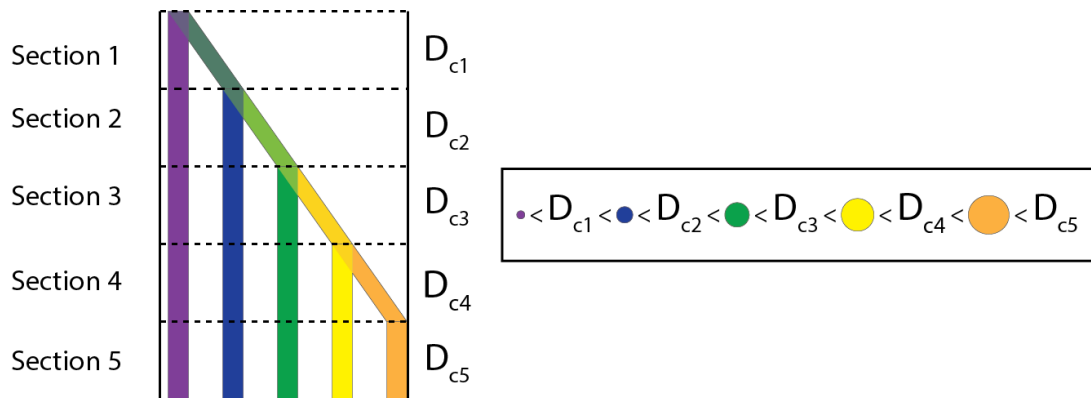


FIGURE 3.4.1: Schematic of a chirped DLD device consisting of 5 sections with incremental critical radii. 5 differently sized particles can be separated in the same device.

3.5 Deformability-based RBC Separation

Deformable particles, such RBCs, deform in the shear of parabolic flow between DLD pillars. The effective size of a deformed RBC is reduced and the deformation extent will determine if the cell trajectory is of zig-zag or displacement mode. As described in chapter 2, the shear-induced deformation is proportional to the flow rate which is proportional to the applied pressure drop over the DLD device. The deformation depends on the mechanical properties of the cell which is variable in a cell population.

Predicting the shear stress onto the particles becomes complex as when the particle itself perturbs the flow profile. Larger particles and higher particle concentrations leading to particle-particle interaction naturally cause larger perturbations. Additionally, softer cells have been simulated to have a lower velocity compared to more rigid cells. This is due to the fact that softer cell has a bigger tendency to end up in the zero-velocity space behind the post. [44]

Another RBC property that is important to deformability-based separation is the time of shape recovery after deformation. If the recovery time is longer than the time a cell takes to pass one post to another, the transit through the array could be affected. Although there have been attempts by different techniques to measure the recovery, the quantitative agreement have been poor with values differing by a factor of 3-5 [45].

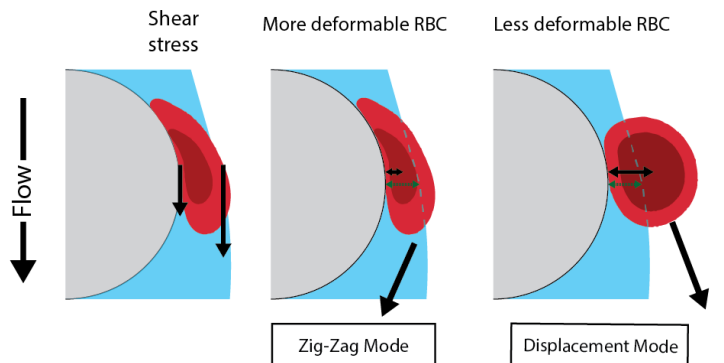


FIGURE 3.5.1: Separation by deformability. Left: illustration of the deforming shear stress. Middle: more deformable RBC ($R_{eff} < R_c$) will zig-zag. Right: less deformable RBC ($R_{eff} > R_c$) will displace.

Chapter 4

Hydrodynamic Trapping

In 2003, Wheeler et al. introduced a new approach to cell trapping, see fig. 4.0.2 [32]. Instead of using complicated systems incorporating external forces such as electrical or optical, they took advantage of the fluid forces already present in the microfluidic channels. When a cell flowed into a trapping cup it was stuck in place. The flowlines that guided the cell into the trapped positions also confined the cell from escaping the trap. The general principle with traps incorporating pores piercing the traps is illustrated in fig. 4.0.1.

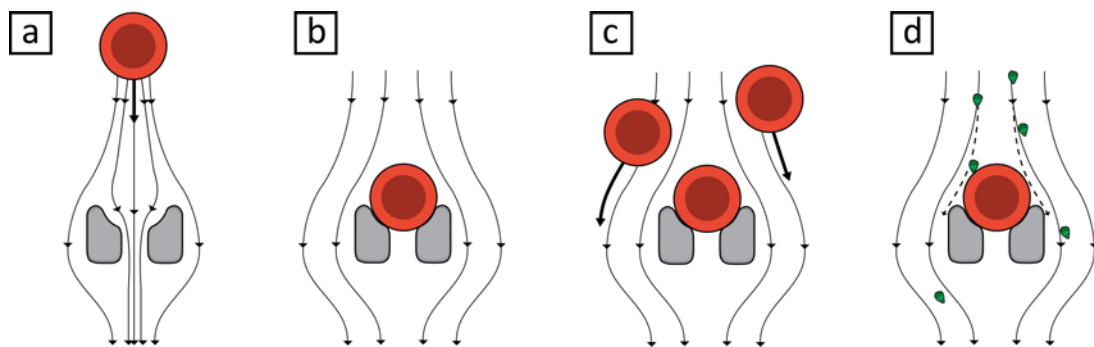


FIGURE 4.0.1: Illustration of the hydrodynamic trapping process. a), b) A red blood cell first get trapped by filling the trapping cup. c) Other RBCs flow past the trapped cell without interference. d) the trapped cell is exposed to a stimulant of some sort, here illustrated with merozoite-stage parasites.

By scaling up the principle from single traps to large arrays of traps one can keep the single-cell control while trapping a large number of cells in parallel. The individual structures either trap one or several cells and are usually set up in a pachinko-style pattern with the rows shifted to each other to allow for a higher trapping efficiency. In 2006, Di Carlo et al. trapped cells using arrays of weir-style traps (traps with a small gap between the trapping structure and the channel roof) to study single-cell enzyme kinetics for different cell types, see fig. 4.0.3 [33]. The flow initially penetrates the empty traps but just like with Wheeler's traps, the flow is diverted once the trap is occupied.

Another example of array-based trapping is by Voldman et. al. where weir-style traps similar to those presented by Di Carlo's group were used for cell pairing and cell fusion [34]. The drawback of the array-approach is that most cells in the cell suspension (80-90%) do not get trapped [46], so an excess of cells is needed. While it can be a problem in some cases, the trapping still gives a representative sample population as the chance of trapping is the same for all introduced cells. Other designs have been made to ensure the trapping of all introduced cells to overcome this problem [47] [48]. While these systems make sure no cells are lost, the extra space needed for the different design results in a lower trap density and overall number of cells.

To efficiently trap cells, the structural parameters of the traps need to be fine-tuned for the cell specific morphology and mechanical properties. As with traps containing a

pore piercing through the structure, the flow can either flow through the trap or circumvent it. The outcome depends on the balance of the hydraulic resistances of both paths.

In this thesis, the red blood cell is the target cell-type for trapping. RBCs are difficult cells to trap due to their high elasticity and non-spherical shape. RBCs can easily squeeze through passages 4 times smaller than their width ($\sim 1-2 \mu\text{m}$) [49], requiring low flow velocities to limit the forces enabling passage through deformation.

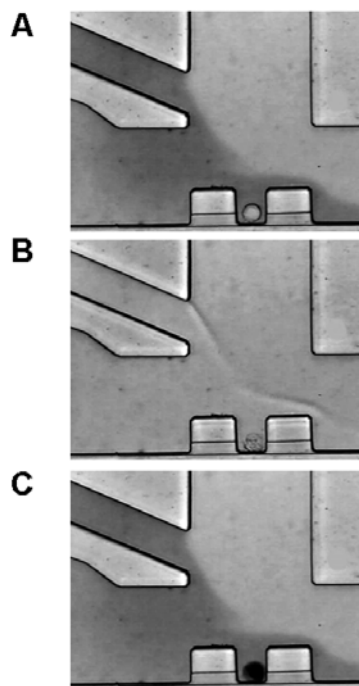


FIGURE 4.0.2: Single-cell trapping in a U-shaped structure. In A and C, the trapped cell (Jurkat T-cell) is exposed to a dye whereas in B the cell is exposed to methanol. Methanol leads to cell death (cell looks deformed in B) and the ability of being stained with the dye (compare the color of the cell of C to A). Reprinted with permission from *Microfluidic device for single-cell analysis*. by Aaron R Wheeler et al. Copyright 2003 American Chemical Society [32].

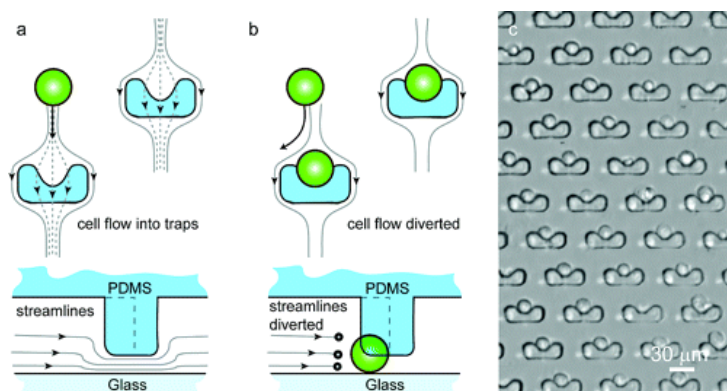


FIGURE 4.0.3: Single-cell trapping using u-shaped weir structures. (a) and (b) shows the principle behind the trapping mechanism. (c) shows an array of trapped cells. Reprinted with permission from *Single-cell enzyme concentrations, kinetics, and inhibition analysis using high-density hydrodynamic cell isolation arrays* by Dino Di Carlo et al. Copyright 2006 American Chemical Society. [33]

Chapter 5

The Red Blood Cell

Red blood cells (RBCs, erythrocytes) circulate through the body, transporting oxygen to and carbon dioxide from cells. RBCs make up about 45% for men and 42% for women of the total blood volume. Other blood cells include white blood cells and platelets, which make up a small percentage. The remaining part of blood is mainly made up of water with suspended proteins, clotting factors, ions, hormones, glucose and suspended gases. Erythrocytes largely consist of the protein hemoglobin ($\sim 35\%$ of the total cell weight [50]) which contains four subunits, each containing an iron-containing heme group (which is also responsible for the red color of blood). Through the Bohr effect, the heme group can absorb and release oxygen at appropriate times during the circulation.

RBCs are produced through the process of erythropoiesis. It lasts for about 7 days and continuously occurs in the bone marrow. After being released from the bone marrow, the RBC circulates the blood stream for 24 hours in the form of an immature red blood cell called a reticulocyte. Reticulocytes constitute for about 1% of the total red blood cell population. When matured, it's known as an erythrocyte ("erythro-" coming from New Latin meaning red). The RBC stays circulating in the bloodstream for approximately 115 days in a normal person. The life span can vary from 70 to 140 days among cells and about $\pm 15\%$ among individuals. The removal from circulation is age-dependant and occur in a nonrandom fashion [51]. The process is not completely understood, but it involves biochemical identification of senescence-associated membrane changes [52]. It has also been suggested that the aged cells are mechanically removed by failing to pass thin endothelial slits ($0.5-1 \mu\text{m}$) in the spleen [53].

5.1 Mechanical properties of red blood cells

When circulating the narrowest capillaries of the body ($2-3 \mu\text{m}$ [54]), RBCs have to undergo severe deformation.

RBC deformability refers to the property of RBCs to change its shape under the influence of an applied stress and returning to its original shape when the stress is released without lysing or rupturing. The deforming stress acting on an RBC can result in cell curvature, uniaxial deformation or area expansion [55].

The mechanical properties of RBCs can be measured by many different techniques, as described in chapter 1. The relevant elastic parameters are bending, area-expansion and shear moduli. The relevant viscous parameters are internal and membrane viscosities and deformation recovery time. The mechanisms underlying RBC deformability is complex and are influenced by many factors.

RBCs are soft, viscoelastic bodies, with both an elastic component that characterize its resistance to deformation and a viscous component that characterizes the rate of deformation. The deformability of RBCs is determined by three properties, the viscoelastic properties of the cell membrane, the RBC morphology, giving its high surface area-to-volume

ratio, and the viscosity of the intracellular fluid, reflecting the hemoglobin concentration of the cell [56]. Other factors also affect the deformability, described below.

5.1.1 The Cytoplasmic Viscosity

The intracellular fluid of the cytoplasm, the cytosol, can be seen as a Newtonian liquid as it does not contain a nucleus or other organelles. The cytoplasmic viscosity, η_i , is dominated by the mean cell hemoglobin concentration (MCHC) [55].

Normal MCHC is around 32 g/dl [55]. Normal η_i has been assessed with membrane fluctuation measurements to around 5-6 mPas [57]. η_i increases with MCHC in a non-linear fashion. At a MCHC of 40 g/dl, η_i is almost quadrupled [55].

5.1.2 Viscoelastic Properties of the Cell Membrane

The cell membrane consists of an outer lipid bilayer, and an inner strengthening network of proteins making up the membrane cytoskeleton. The lipid bilayer is commonly described with the fluid mosaic model [58]. In the model, the bilayer can be seen as a two-dimensional liquid consisting of freely diffusing phospholipids and other membrane components such as proteins and carbohydrates.

The lipid bilayer is anchored to the underlying two-dimensional protein network, the membrane cytoskeleton. It plays the central role of RBC membrane deformability. The network mainly consists of the protein spectrin. Spectrin subunits are joined together through other proteins, making up a triangular meshwork fixed to the lipid bilayer with transmembrane proteins.

The viscous component of the membrane is two-dimensional on an order of $10^9 - 10^{10} Nsm^{-1}$ [59]. It can be qualitatively related to a 3-D bulk viscosity by $\eta_{3D} = \eta_{2D} \cdot 2$, where d is the thickness ($\sim 1-10$ nm). ν_{3D} is then around $10^3 mPas$ [60].

As the intracellular fluid contains no elastic component [55], the energy-storing elastic properties of RBCs is decided by the two-dimensional cell membrane. The shear, bending and area-expansion moduli all refers to the stress to strain ratio of different membrane deformations. Shear is the perpendicular deformation to that of the force where the area extent is maintained. Bending refers to membrane curvature deformation while area expansion refers to an isotropic expansion or compression of the membrane area extent. The shear modulus of RBCs is mainly determined by the spectrin network as the shear modulus of the lipid bilayer is close zero due to its fluidity nature [60]. This can be contrasted to the bending and area expansion moduli which are determined by both the cytoskeleton and the lipid-bilayer. The RBC shear modulus, measured by micropipette aspiration (MAT) [61] [62], magnetic twisting cytometry [63] and optical tweezers [64] has been estimated to 6-10 μNm^{-1} . Average measured values by MAT are around 0 - 19 Nm^{-1} [65] for the bending modulus and 300-500 mNm^{-1} for the area-expansion modulus [61].

5.1.3 Role of RBC Morphology

The special RBC shape, the biconcave disk, gives the cell a high surface area-to-volume (S/V) ratio. The special shape allows RBCs to change shape under stress without increasing its surface area. Expanding the surface area requires far more force than just deforming the cell shape. Besides for enhanced mechanical properties, an increased surface interface enables a higher gas exchange, resulting in a higher amount of oxygen and

carbon dioxide being transported.

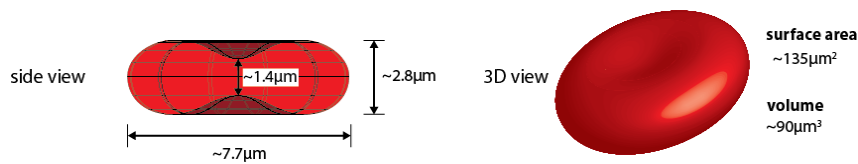


FIGURE 5.1.1: Illustration of a normal red blood cell (discocyte).

The measured dimensions of the RBC differ between sources and measurement techniques. In a large sample ($N_{subjects} = 6$, $N_{cells} = 22985$) RBC morphology analysis study conducted through image cytometry, the mean discocyte diameter was found to be $7.69 \pm 0.43 \mu\text{m}$ [66]. Another source, measured the size with interferometry, (without the diffraction limit of optical microscopy, $N_{subjects} = 14$, $N_{cells} = 1581$) and reported an average diameter of $7.65 \pm \mu\text{m}$. [67] The mean cell volume (MCV) is approximately 94 fL with a mean surface area of about $135 \mu\text{m}^2$ [68], about 40% greater surface area than that of a sphere with the same volume.

A number of agents are able to induce substantial changes in the RBC shape. Anionic amphipaths¹, high osmolarity, high pH, ATP depletion, cholesterol enrichment and proximities to *in-vitro* glass surfaces cause the cell become crenated with outwardly pointed spicules [69]. The crenated cell is known as an echinocyte (echino- coming from Greek meaning hedgehog), seen in fig. 5.1.2 A. Other agents, such as cationic amphipaths, low osmolarity and cholesterol depletion induce a larger inwardly pointed cavity [69]. This cell is called a stomatocyte (Stoma coming from Greek meaning mouth) visualized in fig. 5.1.2. The complete mechanism determining the cell shape and how the shape is

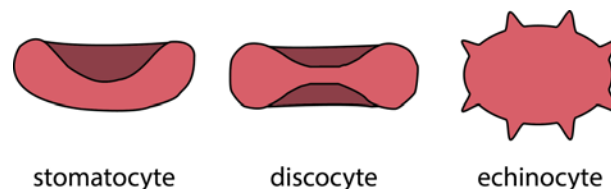


FIGURE 5.1.2: Illustrative cross-sections of a concave stomatocyte, a biconcave discocyte and a spiculated echinocyte.

related to the mechanical properties of the cell is still unknown [60]. The best hypothesis explaining the biconcave shape is the bilayer-couple hypothesis [70]. It also explains the stomatocyte-discocyte-echinocyte sequence where it is proposed that small changes in either side of the two leaflets making up the membrane bilayer would expand either side. If the outer leaflet were to be expanded relative to the inner, the cell would be forced to form convex structures to accommodate for the extra area gained. If instead the inner leaflet would expand, the inverse would happen and concave structures would form. When a cell shape transformation is induced by the above listed agents, the cell deformability also changes as a consequence.

¹Amphipath: Molecule containing both a polar and a non-polar portion of its structure.

5.1.4 Other Factors Impacting RBC Deformability

Temperature affects the viscosity and shear modulus of the cell membrane. From 37°C to 25°C there is no reported change in deformability but below 25°C, deformability is reported to decrease with decreased temperature [71].

Both RBC shape and deformability is dependant on intracellular ATP (Adenosine triphosphate) levels [72] [73].

Alteration of membrane lipids or membrane proteins [74], changes in intracellular calcium ion (Ca^{2+}) concentration [55] or nitric oxide (NO) concentration [75] have also been linked to changes in RBC deformability. Variability of RBC deformability between human subjects are also significant. A number of diseases [56], subject age [76], gender² [77] impact the RBC deformability.

A number of studies have detected losses in surface area, cell volume and deformability during *in vitro* storage [78] [79] [80] [81].

5.2 RBC-age Related Deformability changes

During their circulation, the RBCs are constantly subject to oxidative stress by reactive oxygen species [82]. Mohanty et al. showed that oxidative stress plays a large role in damaging the cell membrane and reducing the deformability of RBCs [83].

There is good evidence that RBCs get denser with age [51]. This density increase is coupled with a reduction in deformability. The changes are thought to be due to both membrane shedding in a process called membrane microvesiculation [84] and due to calcium-induced shrinkage [85] [83].

The mean corpuscular hemoglobin concentration has been reported to increase with 15% as water is lost with aging [86]. A higher MCHC leads to a higher cytoplasmic viscosity in older cells. Williams and Morris anticipate an increase in the internal viscosity by a factor 5 [87].

Although the cell shrinks during its life span ($\sim 14\%$ in volume [51]), the cell area loss by membrane microvesiculation is greater, leading to a smaller S/V [7]. It should be noted that the reported age-related volume changes are less than the range of physiological cell volumes [51].

When fractionating RBCs by density, many studies assume a direct correlation with age when comparing the top and bottom fractions of density-separated RBCs. A recent transfusion study by Franco et al. oppose this linear correlation [51]. Their data indicates that the majority of the density increments occur during the first weeks of the RBC lifespan. Other studies report that hemoglobin losses ($\sim 20\%$) with membrane microvesiculation occurs mainly in the second half of the RBCs lifespan [86] [88]. This supports Franco's claim. Density separation seems therefore be unsuitable if the objective is an isolation of the senescent cell population.

Franco et al. also reported in another study that at the very end of the RBC lifespan, RBCs seem to generally have an irregular morphology [6].

Table 5.2.1 sums up the deformability and size changes of RBCs during *in vivo* aging, described in section 5.2. While these changes are known to occur, the rate or linearity over time of these changes are less known.

²Premenopausal women tend to have on average younger RBCs, and thereby less rigid cells due to monthly menstruation

TABLE 5.2.1: Summary of RBC aging-related DLD trajectory consequences

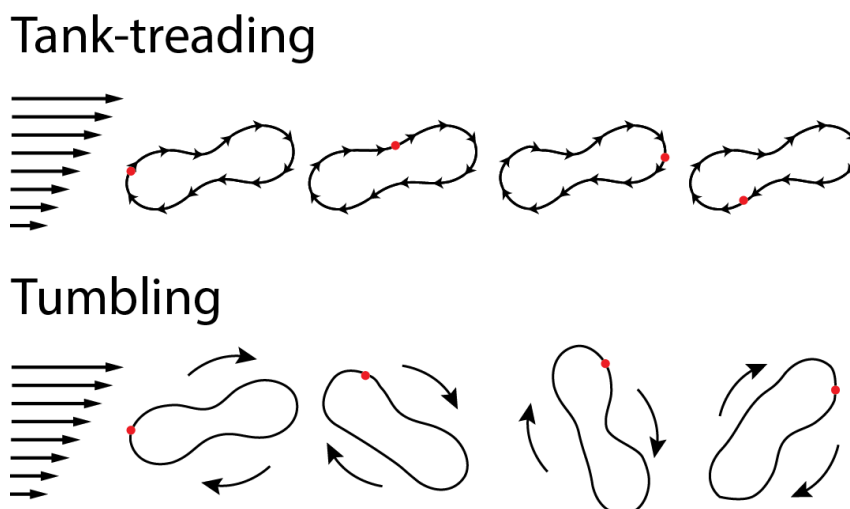
Change	effect to R_{eff}
Membrane elasticity decreases with oxidative damage	larger
Increased MCHC and cytoplasmic viscosity	larger
Cell area loss by membrane microvesiculation, (greater than the volume loss) leading to a smaller S/V.	larger
Cell volume and diameter slightly decreases	smaller

5.3 Dynamics of RBCs in fluid flow

The flow behavior of RBCs is governed by what is the most energetically favorable in a given flow situation. Since we are interested in trapping individual cells and the separation efficiency of DLD is reduced at high cell concentrations, behavioral consequences of cell-cell interactions of whole blood are omitted.

Depending on the flow, the cell will deform in the flow direction to various degrees. When flowing in a capillary (circular-cross section and axisymmetric flow) of 3-13 μm at high shear rates, RBCs are known to form parachute shapes [89] [90].

In a non-axisymmetric flow shear however, uneven shear forces at different membrane positions cause the RBC to rotate around its axis. The motion is reported to change with shear rate and the viscosity contrast, C , defined as the ratio between the intracellular and extracellular fluid viscosities. At high C , as used in this thesis, RBCs have been reported to tumble (flip unsteadily) at lower shear rates and roll at higher shear rates (similar to a rolling wheel). [91] At low C (as in whole blood) and high shear rates, besides the previous two motions, it exhibits a fluid-like tank-treading motion [91] [92]. During tank-treading, the lipid bilayer slides around the cell, against the cytoskeleton, while the cell shape and orientation remain relatively stable. More detailed information about the transitional behavior between the different flow motions including oscillatory motions (swinging) and frisbee-like spinning can be found in literature [93] [91] [94]. Figure 5.3.1 shows examples of flow behaviours of RBCs in a shear flow.

**FIGURE 5.3.1:** Two examples of RBC behavior in shear flow

Chapter 6

P. falciparum

Malaria is an infectious, mosquito-borne disease caused by the protozoan parasites of the genus *Plasmodium*. The most deadly species of the *Plasmodium* genus is the *Plasmodium falciparum* [1] which is the focus of this thesis. The life cycle *P. falciparum* is presented below in fig. 6.0.1.

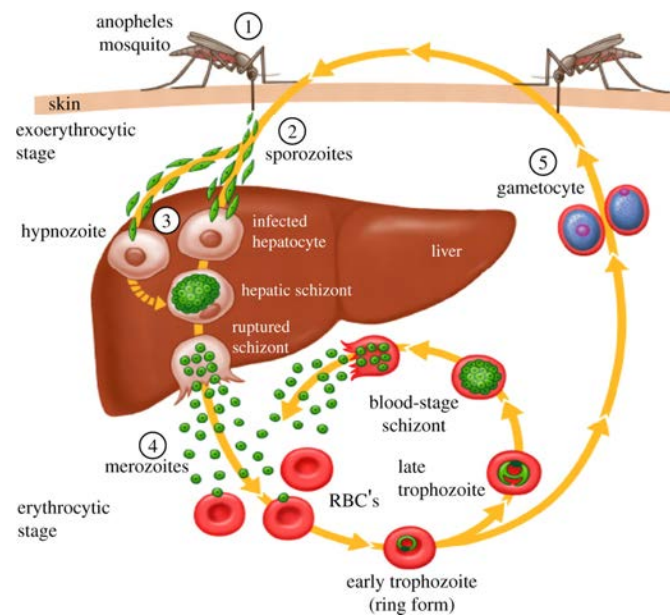


FIGURE 6.0.1: Life cycle of *P. falciparum* inside a human host. (1) A female *Anopheles* mosquito, hosting *P. falciparum* parasites, draws a blood meal through the skin of a human host, and (2) releases sporozoites - motile spore-like *P. falciparum* parasites into the blood stream. (3) Sporozoites migrate to the liver and infect liver cells called hepatocytes. In the hepatocytes, they proliferate asexually, and finally rupture and release merozoite stage parasites into the blood stream (4). This initializes the erythrocytic stage. After an invasion of a RBC, the parasites grow and proliferate (asexually) in a number of stages. It starts with the trophozoite stage and ends in the schizont stage where the RBC finally ruptures and releases more schizonts. (5) Some parasites differentiate to sexual erythrocytic stages (gametocytes). Gametocytes are present in peripheral blood and taken up by the female *Anopheles* mosquito during the blood meal. Figure is open-access and reprinted from [95] in the journal of Philosophical Transactions of the Royal Society B

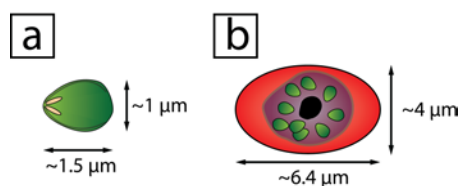


FIGURE 6.0.2: Morphology of *P. falciparum* merozoite (a) and schizont (b)

6.1 Invasion of Red Blood Cells

The invasion starts with *P. f.* merozoites recognizing a RBC host competent for invasion. It then attaches itself by forming a tight-junction¹ to the RBC membrane. After attachment, it reorients and forces itself through the cell membrane via an actin-myosin motor. The entry has been reported to take 30 s, on average [96]. During the invasion process, RBCs have been reported to undergo temporary morphological transformation into echinocytes. After about 5 minutes the shape is returned to normal [96]. Once inside a red blood cell, the parasite divides asexually leading to a schizont containing up to 30 daughter merozoites. After 48 hours following the invasion, the merozoites burst out of the red blood cell to continue further erythrocytic invasions [97]. The invasion cycle happens in a highly synchronous fashion where most of the parasites in blood are in the same stage of development [98].

The invasion is extremely rapid and most of the merozoites lose their invasive capacity soon after schizont rupture. At 37°C, most invasion events have occurred after 10 min. The half life of the invasive capacity has been reported to be 5 minutes. As a proportion of merozoites retain their invasive capacity after 10 minutes, it has been hypothesized that merozoites are not intrinsically shortlived. Instead the decline of invasive capacity is due to multiple mechanisms, including an environmental change [99].

It is important to note that not all invasion attempts are successful. Standard culture invasion rates are known to be 20-40% [99]. Sinha et al. reported that merozoites were unable to penetrate through the membrane of oxidant-exposed RBCs. These cells had damaged cytoskeleton and stiffer membranes [82]. This result indicates that damages induced by oxidative stress during aging may have a role in an age related infection preference. Preference for invading younger cells is in agreement with other studies that report an invasion preference towards the lighter fraction of density-separated cells [3] [4].

6.2 Characteristics of the Schizont and Merozoite stages

Schizonts have a spheroidal shape with diameter of 6.4 μm and thickness of 4 μm , see fig. 6.0.2 [100]. RBC stiffness has been found to increase during the parasitic development inside the cell. A study using optical tweezers has reported up to 10-fold increase in the shear modulus (from 5.3 μNm^{-1} to 53.3 μNm^{-1}) of the schizont-stage infected cell.

Merozoites have an egg-like shape with a tapered front, containing an apicomplexian invasion organelle, see fig. 6.0.2. It has an average diameter of 1-1.5 μm [101]. The magnitude of adhesive force of a merozoite to the RBC membrane has been measured by optical tweezers to be 40 ± 8 pN. Before tweezer-mediated detachment of the complex, RBCs were observed to be elongated by 2 μm [102].

¹Specialized close-fitting connection of two adjacent animal cell membranes

Chapter 7

Materials and Methods

7.1 DLD Device

The DLD device design used, originally designed by Holm et al. [27], can be seen in fig. 7.1.1. The device has a "chirped" design, with thirteen sections placed consecutively, each with a different critical diameter R_c . R_c increases along the length of the device. Each section contains ten DLD periods with constant R_c . The change in R_c has been affected by changing the lateral row shift, $\Delta\lambda$, while holding inter-post gap, G , and post diameter, D_{post} constant. Parameters and the resulting lateral displacement for each array section are presented in appendix D. The D_c ranges from 3 to 9 μm at intervals of around 0.5 μm . Particles larger than 9 μm will be displaced in all sections. Before entering the array, the sample particles flow through a filter which stops any larger (agglomerates, dust, etc.) particles which would otherwise cause clogging and interfere with the separation mechanism in the DLD array. The larger buffer inlet introduces the running solvent or medium, that the displaced cells flow into, while the smaller buffer inlet allows the sample cells to be focused in a streamline. The array edges have been modified, as described in [103], to minimize any flow disruption caused by edge effects. The outlet channels have been designed with equal hydraulic resistance to eliminate any outflow bias from the design.

7.2 Device Design of Trapping Devices

Design drawings were made using the CAD-software L-edit v.16.3 (Tanner Research, Monrovia, California, USA). The channel was fabricated with a depth of 4.1 μm to confine the RBCs to lay flat in the channels. Consequently, the RBCs deform through the trap in the wider position rather than in upright one, see fig. 7.2.1.

The channels are slightly deeper than the average RBC thickness in order to account for cell size heterogeneity; to avoid severe compression of RBCs along the device depth; and the consequent increase in dynamic hydraulic resistance, decrease in convective velocity and clogging.

7.2.1 Trapping Arrays

Each trap has a pore width w , and a circular-arc shaped cup to trap a particle with diameter d_g . The angle, θ , subtended by the arc determines the depth of the trapping cup. The inter-trap distances along a row and column are denoted by d_y and d_x respectively (see fig. 7.2.2).

To avoid trapping of multiple cells in the same cup as in the work by Di Carlo et al. [33], d_g was restricted to 7.5 μm to fit only one RBC. The designs include a w variation of both w (1.5 μm and 3 μm), and θ (149° and 180°), while $d_y = 13.5 \mu\text{m}$ and $d_x = 10 \mu\text{m}$. The single-trap variations can be seen in section 7.2.1.

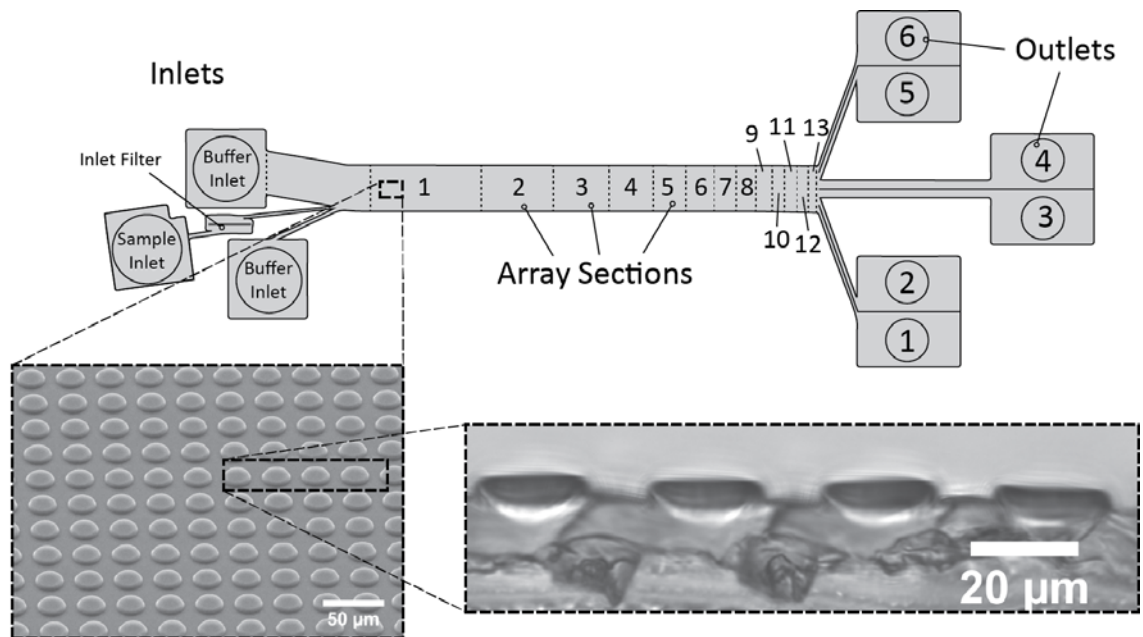


FIGURE 7.1.1: DLD device overview. Critical diameters for the array sections can be found in appendix D. The total device length is approximately 57 mm, fitting onto a normal microscope slide of 76 x 26 mm. Zoom windows (starting from left): Scanning electron micrograph of pillars replicated in PDMS. View is tilted from channel normal about 50°(right). Optical micrograph of PDMS pillar cross-section, pillar height has been measured to 4.2 μm .

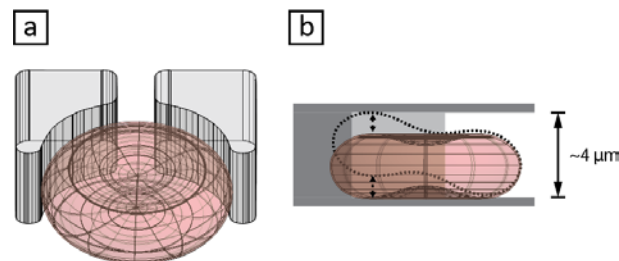


FIGURE 7.2.1: 3D illustration of RBC trapped in a simple single-trap design. The channel depth is reduced to a bit larger the thickness of an RBC. (a) 3D front-view. (b) 2D side-view. The RBC has some wiggling space, illustrated with two sided arrows.

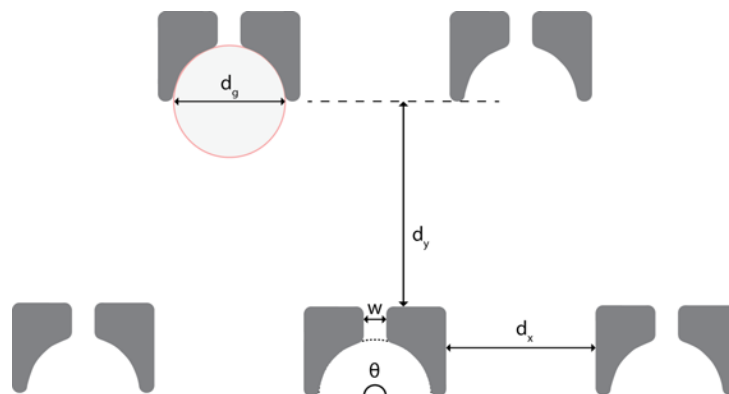


FIGURE 7.2.2: Trap array schematics

All the design parameters were chosen to maximize trapping efficiency (Ratio of trapped cells to that of introduced cells) of RBCs and exposure of the trapped RBCs to the

merozoites in flow. In this trap design, w needs to be low enough to prevent squeeze-through of the RBCs in flow, and high enough to prevent circumvention of RBCs around the traps. Also to note, the resolution of UV-lithography restricts the lower-limit of w . Further, a lower θ would ensure the exposure of the trapped RBC by the merozoites in flow; while a higher θ would secure immobilization in the trap. For the inter-trap distances, the choice of $d_x = 10 \mu\text{m}$ is justified to enable unrestricted flow of an RBC; keep the trap-density high enough; and not place the traps too close, which might increase the shear stress at the trap-pore and lead to RBC squeeze-through. On the other hand, $d_y = 13.5 \mu\text{m}$ was chosen to prevent clogging and enable contact between the trapped RBCs and merozoites.

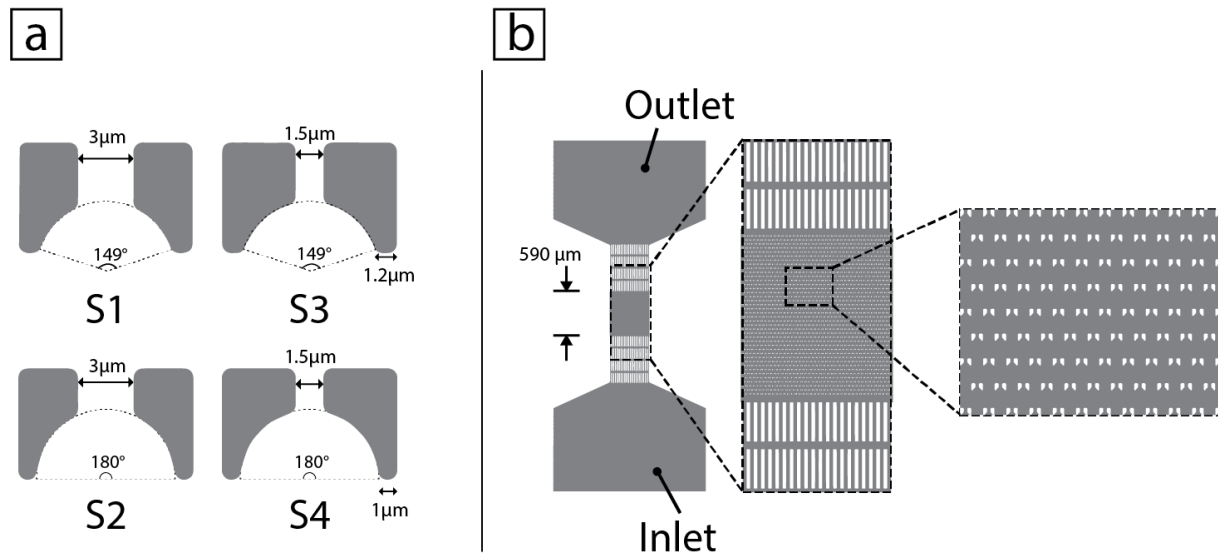


FIGURE 7.2.3: (a) Schematics of single trap variants with angle and pore width. (b) First generation trapping devices. Array of 40×40 traps for all trap variants. Shown here is an example of trap device S2.

Hexagonal-trap arrays

The hexagonal-style traps consists of 6 trapping cups located in an arc allowing for close-contact amongst the cells, see fig. 7.2.4. The design allows for testing of invasion preference by the merozoite. The traps are designed with a pore width of $1.5 \mu\text{m}$ and a cup angle of 180° .

The simpler traps require the parasites to invade the RBC mid-flow, while experiencing high shear stress. While physiological blood stream conditions comprise quite high shear rates as high as 2000s^{-1} (at the walls of the smallest arteries) [104], the effects of shear rate on invasion success have not been studied. A low shear-stress environment could possibly give insight into the invasion mechanism, with only diffusion as means of parasitic transportation between the trapped RBCs.

By placing the cells closer together, the invading parasite has a second choice in the immediate proximity (contrasted to the simpler traps), similar to *in vivo* condition, where the blood stream is filled with cells. This would provide the merozoite a choice, as well as the opportunity to attempt invasion with more than one cell in case of an unsuccessful

invasion. As the merozoites only have a small time window for an invasion [99], the proximity of a second cell could be important for higher invasion rates.

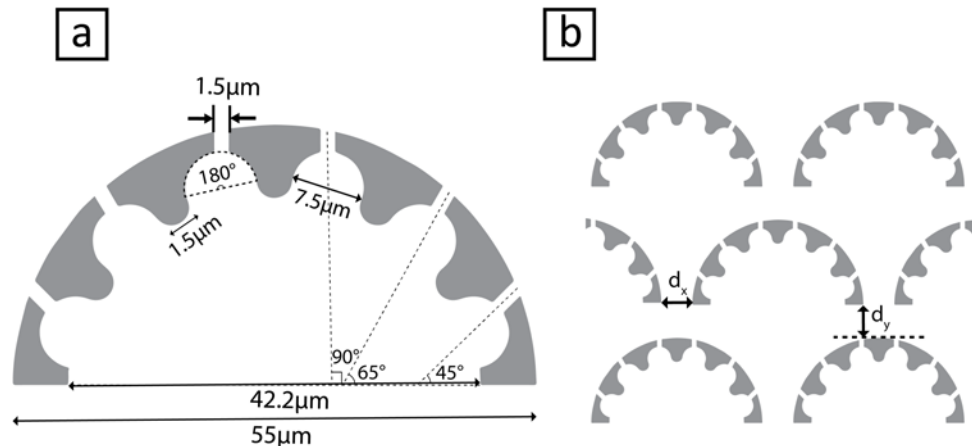


FIGURE 7.2.4: Hexagonal trap schematics. (a) shows the parameters involved for a single-trap whereas (b) illustrates a hexagonal trap array. $d_y = d_x = 10 \mu\text{m}$.

7.3 Trap designs for parasite invasion on-chip

Rather than just cell trapping, this thesis aimed to study parasitic invasion of trapped cells. The task is particularly sensitive, as it is difficult to synchronize schizont rupture *in vitro*, which is important to study preferential invasion while eliminating any temporal artefacts and effects of a heterogenous merozoite density. Also, as discussed before, the invasion capacity of merozoites is short lived. As previously discussed, when burst, the merozoite-stage parasites have only a short time before their invasive capacity fades. After fabrication and testing of the trap array designs, a second trap device generation was designed. The most prominent trap arrays designs (S1 and H3) along with two additional designs (the arc trap and S5) were included.

These devices employed a separate inlet for introducing schizonts, and contained a post-filter of 3 μm pores to hold the schizonts in place before rupture. This pore width was thought to be a good distance as it has been shown to obstruct schizonts in similar experiments. In one study found, schizonts were unable to pass single constrictions of less than 3 μm [105]. Schizonts have also been shown to pass constrictions as small as 1.5 μm but this needed a significant pressure (200 bar) drop over a single path [106].

After schizont-rupture, the smaller merozoites can pass rapidly through the filter and subsequent channels, and interact with the trapped RBCs in the downstream-placed array.

7.3.1 Arc trap

A problem that arises with trapping arrays is the lack of equal chance for a trapped cell of being encountered by a flowing parasite. The first rows will always be encountered first, thus, a gradient of encountering events forms. While this design still can give information about the dynamics and preferential infection, it is more difficult to extract as cells can be invaded by multiple parasites or completely miss being encountered due

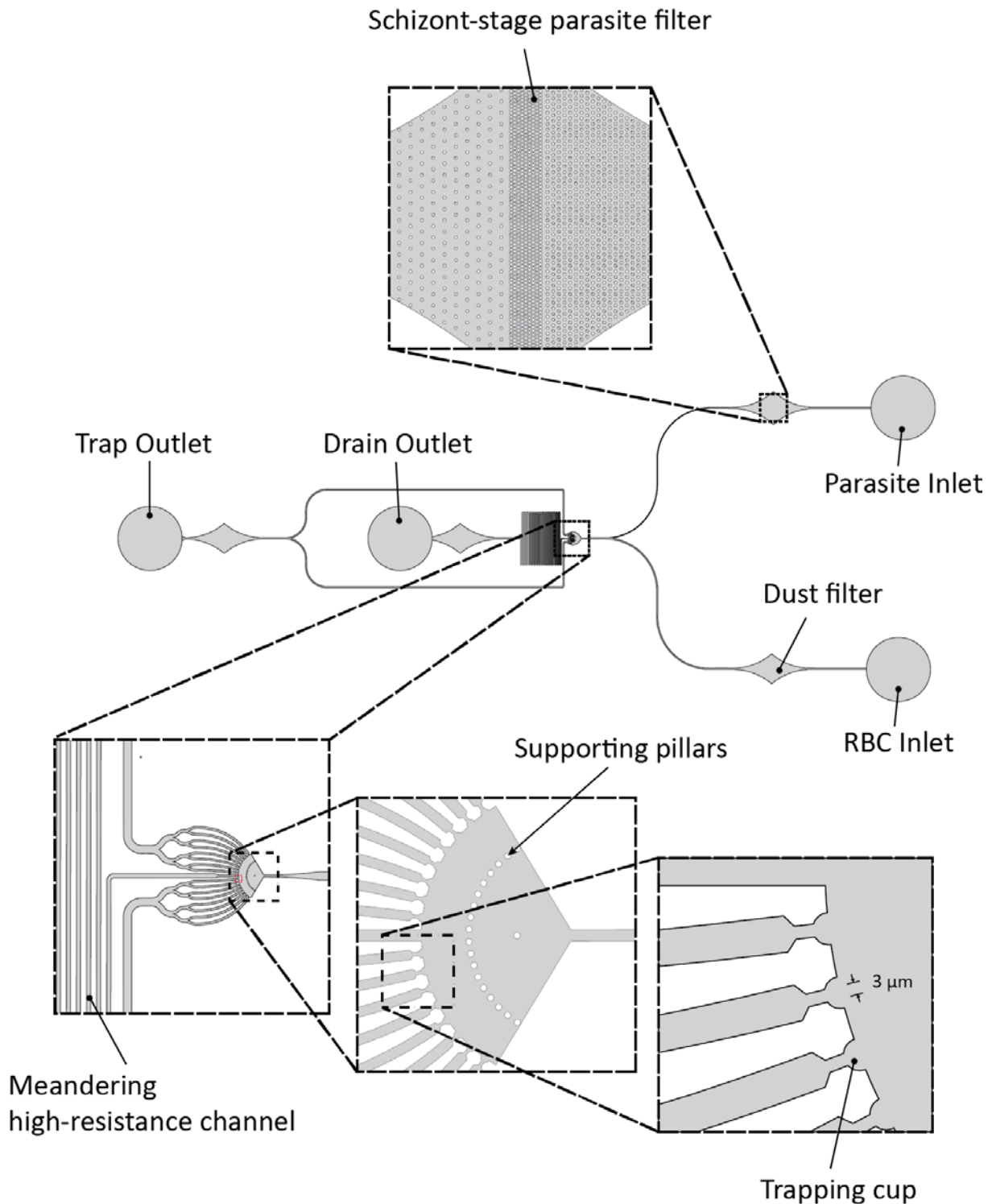


FIGURE 7.2.5: Schematic of the device incorporating the arc trap. The other parasite-infection on chip devices have identical layout except a drain outlet and a meandering channel (see fig. 7.3.1). The trapping arrays are positioned at the location of the arc trap.

to being positioned further downstream. Optimally one would like to introduce one and only one parasite to several RBCs in a massively parallel fashion. While this is difficult to accomplish, a compromise has been designed, see fig. 7.2.5. It is a trapping design where multiple trapping cups are placed at regularly spaced intervals in an arc. The

pore width of the traps is $3\ \mu\text{m}$. Supporting pillars have been added to the open arc area to prevent a channel collapse due to the large area. The channels following the individual cups are calculated to have equal hydraulic resistance to abide for equal chance of being encountered by parasites. The design assumes a small flow around the trapped RBCs through the pore of each trapping cup. To clear the area from excess cells, a high-resistance meandering drain channel is present at the middle of the arc. When all RBCs are trapped, the pressure to the RBC inlet is lowered and the parasite inlet is raised. The excess cells will be flushed through the meander and the system is awaiting parasites from the parasite inlet.

7.3.2 No-pore Trapping Array

A second single-trap design variant, denoted S5, can be seen in fig. 7.3.1. It lacks a pore, similar to that of the original hydrodynamic trap by Wheeler et al. [32]. It has a deeper trapping cup with an cup angle of 180° . The purpose of this trap design is to reduce any eventual RBC shear deformation otherwise present with the trap variants with pores. Possibly, the RBC deformation could negatively affect the invasion process.

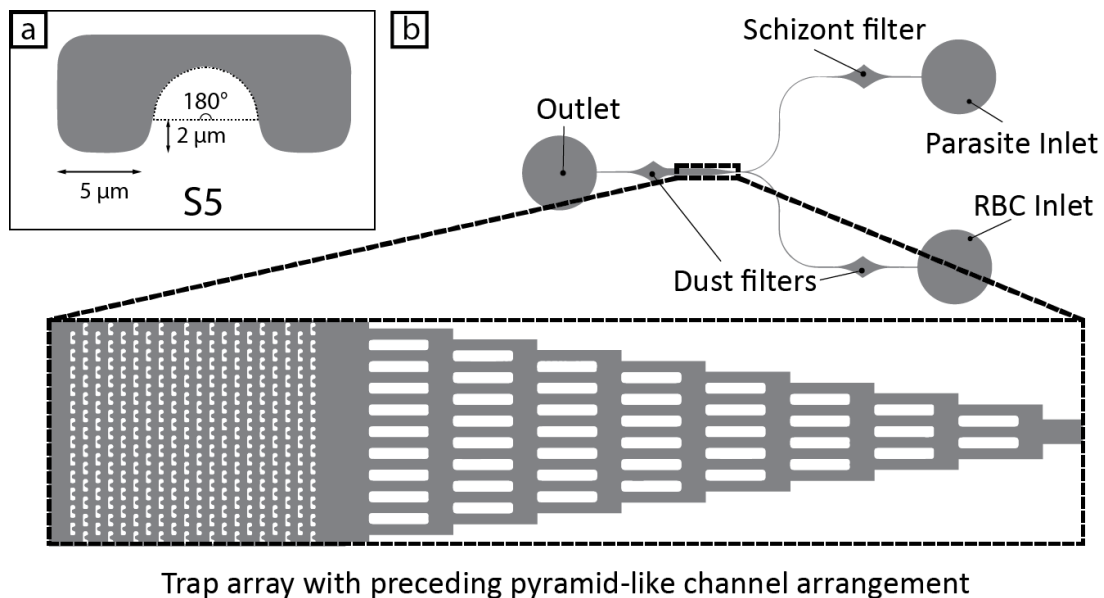


FIGURE 7.3.1: (a) Schematics of trap design S5. Row and column distances (d_x and d_y) are equal to $10\ \mu\text{m}$. (b) Second generation device schematics.

7.4 Numerical Simulation

Due to the complexity of the partial differential equations of microfluidics and the asymmetry of real-life conditions, numerical solutions are used to predict the flow behavior. In this thesis, the finite-element method (FEM) was employed by using the simulation software COMSOL Multiphysics 5.1 (COMSOL Inc. Stockholm, Sweden). FEM divides the continuous equations governing microfluidics into a matrix consisting of small and discrete chunks called finite elements. The calculation time and the problem size relies heavily on the number of elements the matrix is divided into. In the simulations, creeping flow (Low Re) was employed with no-slip boundary conditions at the walls. Periodic flow

conditions have been applied to make the simulated trap array infinitely large. By measuring the flow velocities of small polymer beads ($1\ \mu\text{m}$ in diameter) inside the devices, the pressure drop over an individual unit cell can be estimated for a given pressure applied to the inlets. As the beads are small and rigid, they follow the streamlines rigorously at high flow rates and can give good approximate values of the flow profile.

7.5 Device Fabrication

The microfluidic devices were made in the silicone rubber Poly-Di-Methyl-Siloxane (PDMS, Sylgard 184, Dow Corning) using the technique called replica molding. PDMS is a soft, elastomeric polymer with many advantages. It's biocompatible [107], transparent for relevant wavelengths (240 nm - 1100 nm) and cheap. The greatest benefit of fabricating of PDMS is the ease of rapid prototyping it allows. The mold required for the process can be made with UV-lithography in a day and ready-to-use devices can be made from that mold in about 6 hours. The basic fabrication steps can be seen in fig. 7.5.1 and the detailed fabrication protocols can be found in appendices B and C.

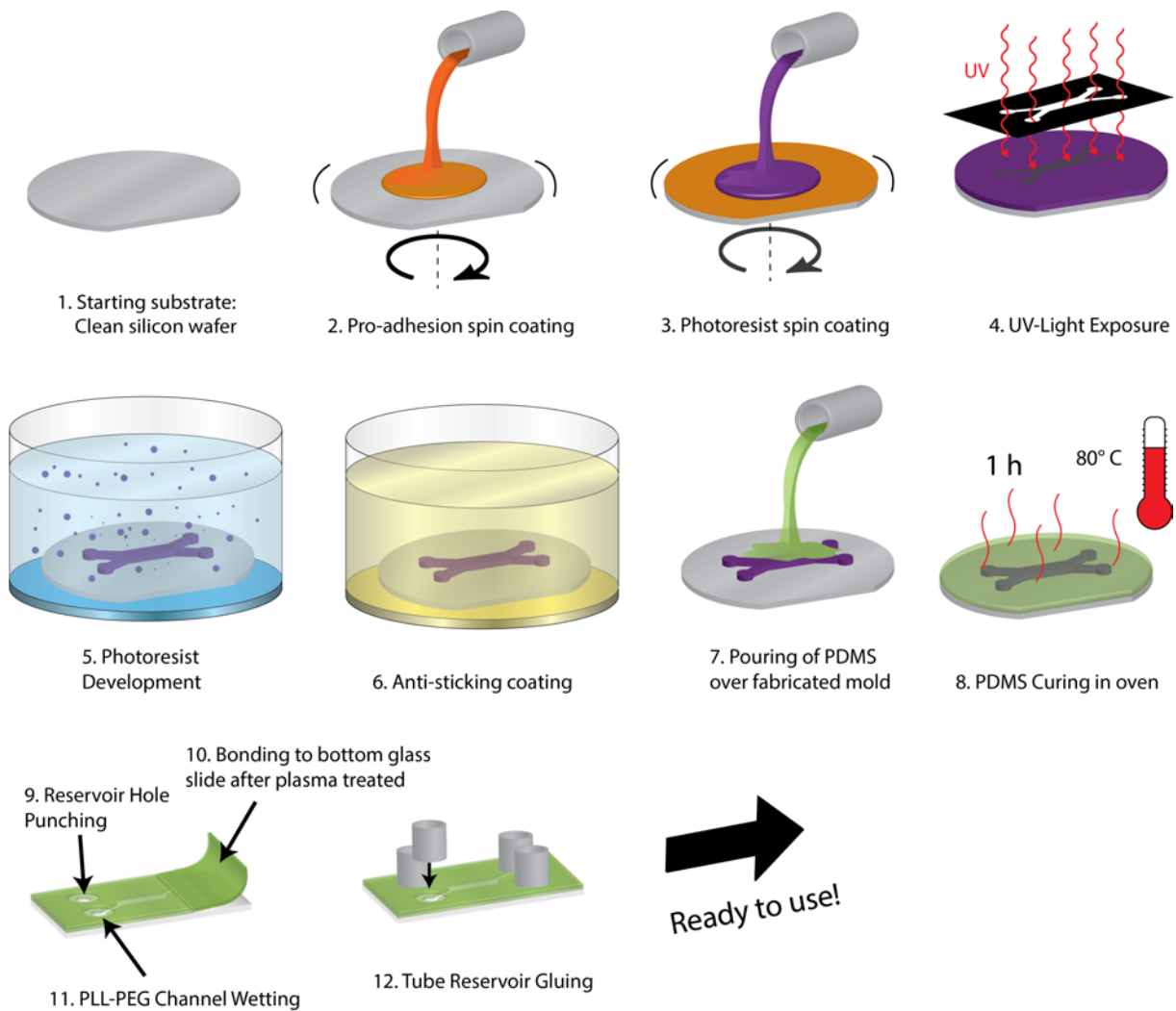


FIGURE 7.5.1: An overview of the device fabrication process.

7.5.1 UV-Lithography

The mold is created by transferring a fluidics pattern on a chromium mask to a photoresist layer. The mask containing the designed patterned was manufactured by a photomask-supplier where it was made with a laser writer. The photoresist making up the mold is first spin-coated onto a silicon wafer substrate. The photoresist is then subject to UV-lithography. The photoresist used, SU-8 (MicroChem, Newton, MA, USA), is a negative photoresist, meaning that the parts exposed to UV-light will be cross-linked whereas unexposed parts get washed away in a development step.

Several baking steps are included into the process, dehydrating the sample at appropriate times, which are excluded from fig. 7.5.1 for simplicity. These include soft-baking, prior to UV-exposure, post-exposure bake, following UV-exposure and hard-baking, following resist development.

7.5.2 Soft Lithography

PDMS was prepared by mixing its base and its cross-linking agent carefully and then degassed it in a vacuum chamber for 30 minutes. The prepolymer was then poured over the SU-8 mold and cured in an oven for generally 1 hour at 80°C. It was then carefully peeled off the mold and the relevant channel system was cut out with a scalpel. Reservoir holes (2 mm) were punched with a flat-tip needle at all inlet and outlet regions. The PDMS slab and a PDMS spin-coated glass substrate(75 x 25 mm) were treated with oxygen plasma for 30s at 750 W) to make the surfaces hydrophilic and make covalent bonding of PDMS to PDMS possible. Both the PDMS parts were then bonded tightly together.

The PDMS surface hydrophilicity decreases rapidly. It recovers most of its hydrophobicity by 15 minutes unless a hydrophilic liquid (water) is added soon after the treatment. [108] To prevent the recovery from occurring, immediately after bonding, the devices were filled with an aqueous solution. The solution is made up of 0.2% PLL-g-PEG (poly[l-lysine]-graft-Polyethyleneglycol, SuSoS AG, Dübendorf, Switzerland) in deionized water. The substance is added to reduce the adsorption of proteins and cells to the inner surfaces of the device. It consists of Polyethyleneglycol (PEG) grafted to PLL (poly[l-lysine]). PEG is known to suppress the adhesion of cells and proteins to PDMS. PEG is also both non-toxic to the cells and is a widely used surface modification compound. [109]The positively charged PLL backbone readily adsorbs to the negatively charged PDMS surface induced by oxygen plasma.

The fabricated device is stored in a humidified chamber for up to 48 hours at 8 °C before use.

7.5.3 Fabrication Process Troubleshooting

UV-lithography is a crucial and sensitive fabrication step, that determines the quality of the required micro-structures. To obtain suitable and intended trap structures, considerable amount of effort was invested at this fabrication step. This section aims to discuss the encountered issues during UV-lithography, as well as the downstream fabrication processes, and to address the problems in a strategic manner.

During the UV-lithography fabrication, the thin spin-coated photoresist frequently released from the substrate. As this was thought to be due to internal stress created during

the rapid temperature rise during post-exposure-baking, a more gentle temperature rise, with a 20 min ramp was tried. This, however, led to further substrate lift-off. Subsequently, an additional ultra-thin adhesion layer of OmniCoat (MicroChem, Newton, MA, USA) was applied prior to the photoresist. This led to prevention of the lift-off of the substrate during development.

The fabrication of the small and complex trap features in a thin mold ($\sim 1 \mu\text{m}$) required an optimization of the photolithography process. To achieve the desired photoresist thickness, which is identical to PDMS channel depth, the spin speed was varied from 1500 to 3000 RPM.

The designed traps have sharp-edges and small ($\sim 1 \mu\text{m}$) segments, making them difficult to fabricate. The particular mask aligner used for UV-treatment can go down to a lateral resolution of about estimated $1 \mu\text{m}$ before defects due to diffraction effects become too great. At these resolutions, it is very difficult to achieve vertical side walls. Some curvature of the walls is therefore to be expected. To attain an accurate replication of the mask design to the photoresist, the UV-exposure dose time and development time were varied for the specific photoresist thickness used.

Due to the flexibility of PDMS, there is a risk of collapse of the channel. This can happen when the width to height aspect ratio is above 10:1. For the DLD-device, the aspect ratio at the reservoir areas and the connecting channels from the inlets was 12:1, leading to collapse of shallow channels. To counteract the frequent collapsing, the PDMS stiffness was modified. The PDMS was made stiffer by prolonged curing duration ($\sim 4\text{-}24\text{h}$) and by lowering the ratio of the base and cross-linking agent mixing ratio to 8:1 from 10:1. At a 10:1 ratio, collapse of the channel was observed at channel depths of $3.1 \mu\text{m}$, $3.5 \mu\text{m}$, $3.8 \mu\text{m}$ and $4.2 \mu\text{m}$ while $5.1 \mu\text{m}$ deep channels survived. For a ratio of 8:1 and prolonged curing duration, $4.2 \mu\text{m}$ deep DLD devices generally survived collapsing if only a careful light touch was applied after bonding to the PDMS substrate.

Other problems frequently encountered during experiments were channel blockage, either by air bubbles, dust particles or fibers. Even with plasma-enhanced bonding, the bonding sometimes failed. Insufficient gluing, leading to leakage was also commonly seen. To prevent leaking from happening during experiments, a gluing reinforcement step was added to the fabrication process.

7.6 Sample Preparation

A small blood sample (20-50 μL) was drawn via finger-prick method using a lancet. To prevent coagulation, it was immediately mixed with a buffer containing an anticoagulant - either autoMACS[®] (Miltenyi Biotec, Lund, Sweden) containing the anticoagulant ethylenediaminetetraacetic acid (EDTA); or citrate phosphate dextrose adenine (CPDA) containing citrate ions. EDTA has a stronger potency (irreversible) than citrate (reversible) but is possibly more cytotoxic. CPDA was therefore used for any experiments involving parasites while EDTA was used for device testing. To deal with the weaker anticoagulation of CPDA, number of washing steps were employed to remove any remaining platelets that could otherwise start the coagulation process. When using autoMACS[®], the wash-

ing was carried out in one centrifugation step. The complete blood preparation protocol can be found in appendix A.

1 μ m polymer microspheres (Duke Scientific Corp., Palo Alto, United States) were used to mimic merozoites in the devices.

7.7 Parasite Culturing

Plasmodium falciparum was cultured by our collaborators¹ in 5% hematocrit in a glass flask of 37°C with a gas atmosphere of 5% CO₂, 90% N₂ and 5% O₂. The culturing medium consists of RPMI (Roswell Park Memorial Institute) 1640 tissue culture medium supplemented with 0.5% (w/v) AlbuMAX II. Magnetic isolation of schizonts [110] were used to generate a high parasitemia (~ 95-99%) and a highly synchronized culture (synchrony window of ~ 4 hours).

7.8 Experimental setup

The experimental procedure starts with mounting the device on the inverted microscope and connecting the inlet reservoir tubes to a pressure control system. The running channel temperature is around 24-25°C. To ensure a cell-friendly liquid environment in the channels, the channels were first flushed with the running buffer for 10 minutes at 1000 mBar. The running buffer in the microfluidic devices was either autoMACS[®] or the parasite culturing medium. The reservoir tubes were washed several times when changing the medium to ensure no traces remained of the previous liquid. Any liquid (except the blood sample) inserted into the device was filtered with a 0.2 μ m syringe filter to remove any particles that could otherwise clog the system. To make sure no bubbles were introduced into the channels, the sample was always carefully aspirated near the channel entrance in the tube reservoir. After flushing the running buffer, the sample is pipetted into the sample inlet. To prevent sedimentation in the reservoir, a 2 mm magnetic polystyrene bead was placed in the inlet reservoir. It was stirred every 5 min by an externally applied magnetic field. Data acquisition was made with one of several cameras mounted on the microscope. The complete laboratory setup can be found in fig. 7.8.1.

7.8.1 Parasite experiments

The experiments involving parasites were conducted in a Biosafety Level 3 laboratory at Department of Molecular Biosciences, Wenner-Gren Institute, Stockholm University, Stockholm, Sweden. The experimental setup differed slightly. As the malaria parasites is a biological hazard, special precautions were taken. Every tool was wiped clean with 70% ethanol before and after usage. The parasites were preloaded into the device in a laminar hood of a lab of biosafety level 3.

A stage heater capable of heating the microfluidic chip to around ~ 37°C was mounted on the microscope to ensure physiological temperatures optimal for the parasites.

The applied carrier gas differed from the normal N₂ gas. Instead, CO₂ was applied as the carrier gas by the pressure control system.

¹Dr. Lisa C. Ranford-Cartwright & Laura Ciuffreda at University of Glasgow.

The carrier medium in the devices were always the parasite culture medium. Blood used in the experiments was drained from a vein rather than a finger prick from a healthy anonymous volunteer. CPDA was used as anticoagulant and the blood sample was thoroughly washed in standard clinical protocols before usage. Initially, blood stored for 2 weeks after collection was used for the experiments. However, at a later stage, freshly collected and processed blood was used to prevent any effects due to *in vitro* aging.

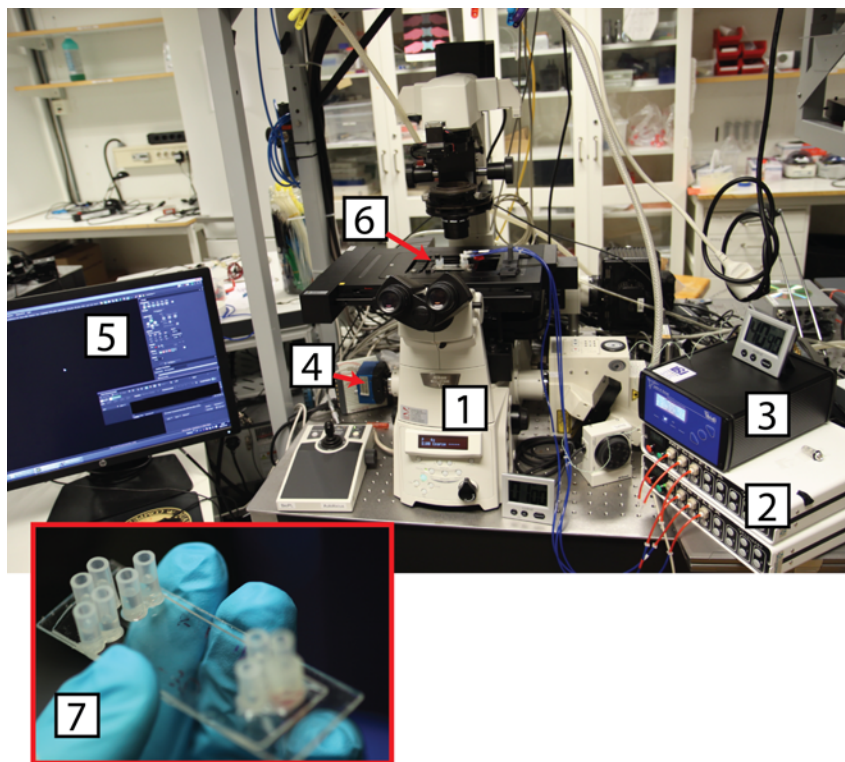


FIGURE 7.8.1: General experimental setup. (1) Nikon Eclipse TE2000-U inverted microscope (Nikon Corporation, Tokyo, Japan), (2) MFCS-4C or MFCS-8C pressure controllers (Fluigent, Paris, France), 0-1000 mbar. (3) Thermocouple temperature sensor (ibidi GmbH, Planegg, Germany)(4) Camera used for image capture. Camera on the photo is a high-speed EoSens mini MC-1370 camera (Mikrotron GmbH, Unterschleissheim, Germany). Other cameras used were an Andor Ixon EMCCD camera (Andor Technology, Belfast, Northern Ireland) and a DFK MKU130-10x22 (The Imaging Source Europe GmbH, Überseetor, Germany) (5) Computer connected to the microscope. (6) Mounted chip. (7) Zoom-in on a DLD chip with 9 tube reservoirs.

7.9 Sterility

It is important that the DLD-fractionated blood sample is sterile. If any microorganisms would be present and start growing in the subsequent culturing with *P. falciparum*, the analysis of infection would be hampered. To prevent any contamination, channels were first flushed with ethanol (70% v/v) for 5 minutes with 1000 mBar applied to the inlets. Equipment that would come in contact with the sample or the running buffer were autoclaved beforehand (120°C, 2-5 bar) or if autoclaving were not possible, such as for plastic pressure gas connectors, thorough washing with ethanol was carried out.

7.10 Data Analysis

Captured images were analyzed using ImageJ v. 1.50b (Public Domain, developed at National Institutes of Health, Maryland, United States). Quantification of the DLD outlet distribution first involved subtracting the median-background from a video taken of the outlet area. The frames were then converted to a binary format and summed together to quantify the intensity at each location over the duration of the video. The process can be visualized in fig. 7.10.1. The quantification was conducted like this rather than tracking each particles with a tracking algorithm due to the high cell densities with overlapping trajectories making tracking difficult. The drawback of the method is that slower-moving particles will have a greater contribution to the distribution than faster-moving particles as slower-moving particles will be captured in more frames.



FIGURE 7.10.1: Image analysis of outlet trajectories. (a) Single image frame from a video captured with a high-speed camera. (b) Frame from (a) which first has had its static background subtracted and then been converted to a binary format at a grayscale pixel threshold with no noise. (c) Sum of 15 000 frames processed like that in (b). Red line marks the location of where the pixel intensity was extracted.

The sizes of RBCs following DLD separation was measured using optical microscopy, where the diameter was defined as the distance between the two pixel intensity lows of the RBC edges (see fig. 7.10.2). Prior to measurement, the RBCs were first aspirated in a small sample volume (5 μL) from the DLD reservoirs onto a glass slide.

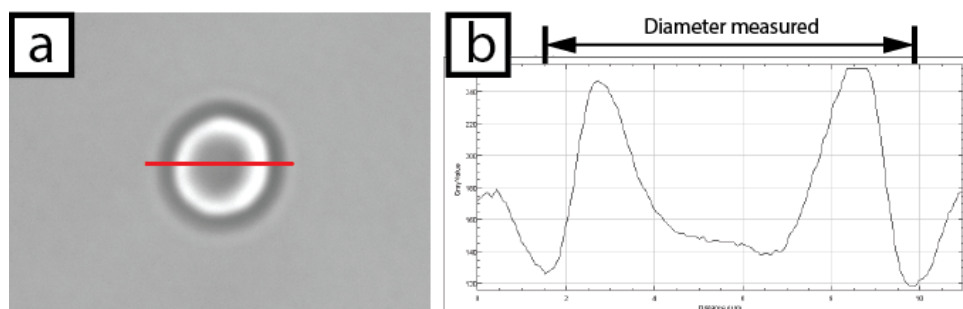


FIGURE 7.10.2: RBC geometry analysis. (a) A micrograph of a red blood cell placed on a glass slide. (b) Pixel intensity profile along the length of the RBC (the red line)

Chapter 8

Results and Discussion

8.1 Deterministic Lateral Displacement

8.1.1 RBC Deformation

The numerical simulation results of the flow inside DLD can be seen below in fig. 8.1.1. The resulting flow velocity and shear rate is compared for pressure drops of 100 mbar and 500 mbar. At a higher pressure drop, the overall velocity magnitude is higher and so is the shear rate at the pillar walls. As the shear strain is proportional to the shear rate, RBCs should deform to a larger extent at higher pressure drops.

Cell deformation for four chosen pressure drops can be visualized in fig. 8.1.2. The presented cells are of similar size and shape (discocytes), although their deformability could slightly differ. Just like with the simulation results below, the deformation generally increases with a higher pressure drop for similar cells. At a low driving pressure of 10 mbar, only a faint deformation is visible. When increasing the driving pressure, the deformation and thus the effective size of the cells inside the device decreases.

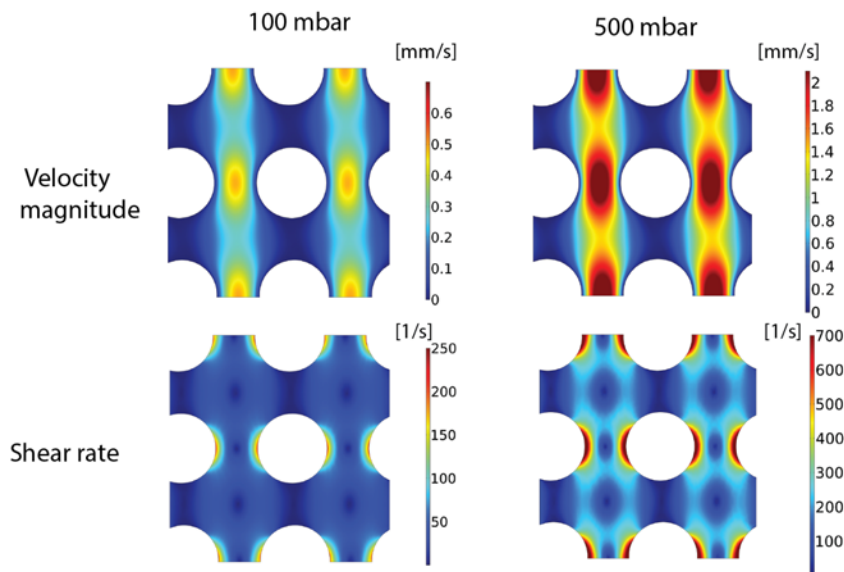


FIGURE 8.1.1: Simulation of shear rate and flow velocity in an DLD array with the following parameters: $G = 12 \mu\text{m}$, $\lambda = 32 \mu\text{m}$, $D_{post}=20$, $\Delta\lambda = 0.8 \mu\text{m}$.

8.1.2 RBC Fractionation

Figure 8.1.4 shows the distributions of cells at the outlet of the DLD device for different driving pressures. The width of the distributions can be compared to the inlet stream width of $\sim 100 \mu\text{m}$. The spreading can be attributed to a variation in size and deformability

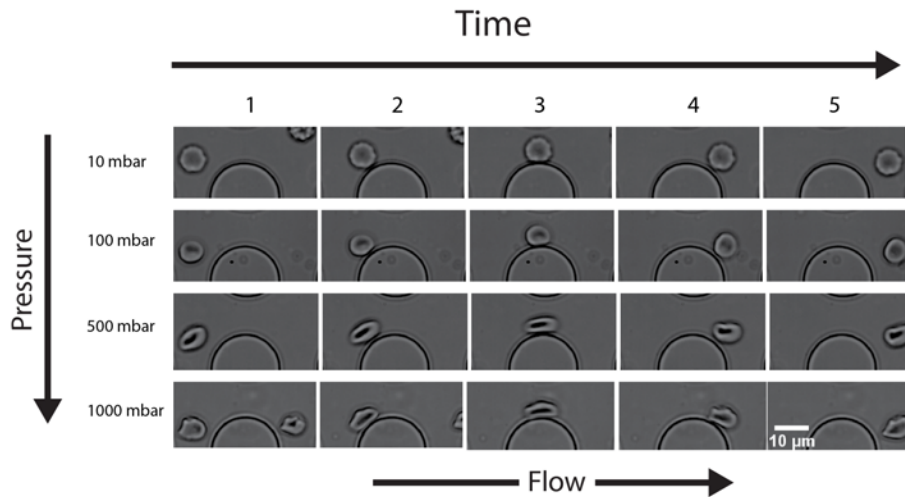


FIGURE 8.1.2: Deformation of RBCs in section 2 of the DLD array at four different pressures. Frame time steps are for 10 mbar - 210 ms, 100 mbar - 28 ms, 500 mbar - 4.5 ms, 1000 mbar - 2.48 ms.

as diffusion is low, Pe of $\sim 3.3 \cdot 10^4$ for a driving pressure of 100 mbar, assuming a flow velocity of $0.5 \mu\text{m}/\text{s}$. At low driving pressures and consequently little cell deformation, the distribution can be attributed mainly to variation in size. When raising the driving pressure, the distribution is shifted towards zig-zagging rather than displacing, with the impact of deformability in the separation. Larger cells with the same deformability as smaller cells could (depending on the applied pressure) still have different effective sizes and arrive at different outlet positions. Thus, the technique cannot completely eliminate size variation when separating by deformability. However, if the size variation is smaller than the variation in effective size by deformation, fractionated subpopulations, and especially the extreme fractions, would still have a differing deformability.

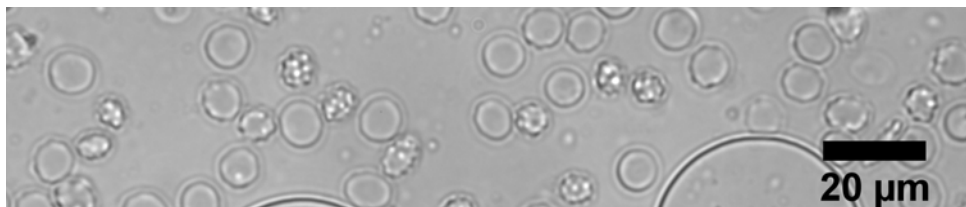


FIGURE 8.1.3: Various RBC morphologies in inlet area. Both crenated echinocytes and regular discocytes can be seen.

A great number of RBCs (both uninfected and infected cells) underwent echinocytic shape transformation inside the channels (see fig. 8.1.3). Cells that become echinocytic have a more spherical shape with a reduced cell diameter as described in chapter 5. As reported by [22], despite having a smaller diameter, echinocytes generally have a larger effective size in shallow-channel DLD at high driving pressures compared to discocytes with the same cell volume. With a mixed shape population, deformability fractionation is dampened by a simultaneous fractionation in differing morphology. It is also important to note that the transformation is not binary but there is a continuum of shapes ranging from the discocyte to the most crenated echinocyte.

It is possible that even if all cells underwent shape changes, deformability differences between young and old cells would still be significant. The tendency to change into an odd

could possible also be an indicator for the cell age as discovered by Franco et al. [6] for the very old cells. Differences in both hemoglobin concentrations and viscoelastic properties of the cell membrane remain with the shape changes. DLD could then still be used to fractionate the RBCs into differing ages despite shape transformations.

As discussed more thoroughly in the next section, the shape changes are thought to be due to local high pH at the channel surfaces, referred to as the “glass effect” as it was first discovered to appear near glass surfaces. As the shape transformation by the “glass effect” is reversible [111], the *P. falciparum* infection rates of the fractionated cells could still be compared without having to consider invasion interference by an altered cell morphology.

The echinocytosis was generally observed to occur in the inlet region of the device (see fig. 8.1.3). The flow rate and thus the residence time is high in this location as the cells first have to pass the narrow filter to reach the array (see fig. 7.1.1). At low flow rates and high cell concentrations as used in the experiments leading to fig. 8.1.4, the residence time is especially high. As higher driving pressures in the experiments of fig. 8.1.4 were used after the lower, shape transformations of the cell had already occurred for higher driving pressures experiments. By redesigning the inlet area, the in-channel residence times could be reduced and possibly also the degree of transformation.

Figure 8.1.4 also shows the outlet reservoirs the cells are collected in after fractionation. To study the highest possible invasion efficiency contrast of deformability-separated cells, it is preferable to compare the extreme cell fractions (with highest and lowest deformability). For the given device design, only at the pressure of 500 mbar, isolation of the extreme fractions into separate outlets is possible. At even higher pressures, where the impact of deformability in the separation process could be even higher, the distribution is shifted into the leftmost outlets where the cell population is divided only into two fractions.

8.1.3 High-pressure Fractionation

Figure 8.1.5 shows the outlet distribution of an RBC cell population with a driving pressure of 500 mbar. The cell concentration has been lowered from 20 x whole blood dilution to 40 x. In addition to this, cells have only been flowing into the device at high pressure (500 mbar), lowering the residence time significantly from the previous experiments.

As a consequence, the presence of shape transformed cells is considerable lower. From an estimated 60-70% echinocytic cells in fig. 8.1.4 to 35%, 10% and 4.8% in outlet 1-3 respectively. This also shows that echinocytes are smaller than discocytes in this device (as mentioned above)

About 1 % of the cells flow into outlet 1 and about 5% of the cells into outlet 3. In fig. 8.1.6, the size distribution of the cells separated into these outlets can be seen. The deformability-based separation of RBCs in DLD is limited by a large variation in cell size. The cells in outlet 1 have a smaller cell radius mean (3.76 μm) than the control (4.00 μm) and the cells in outlet 3 have a larger mean (4.25 μm). The distribution is wider in outlet 1 than both the outlet 3 and control sample (Standard deviations are 0.57 μm , 0.38 μm and 0.38 μm respectively) The larger distribution width of outlet 1 still remains at 0.57 μm when taking account of the large percentage of echinocytes.

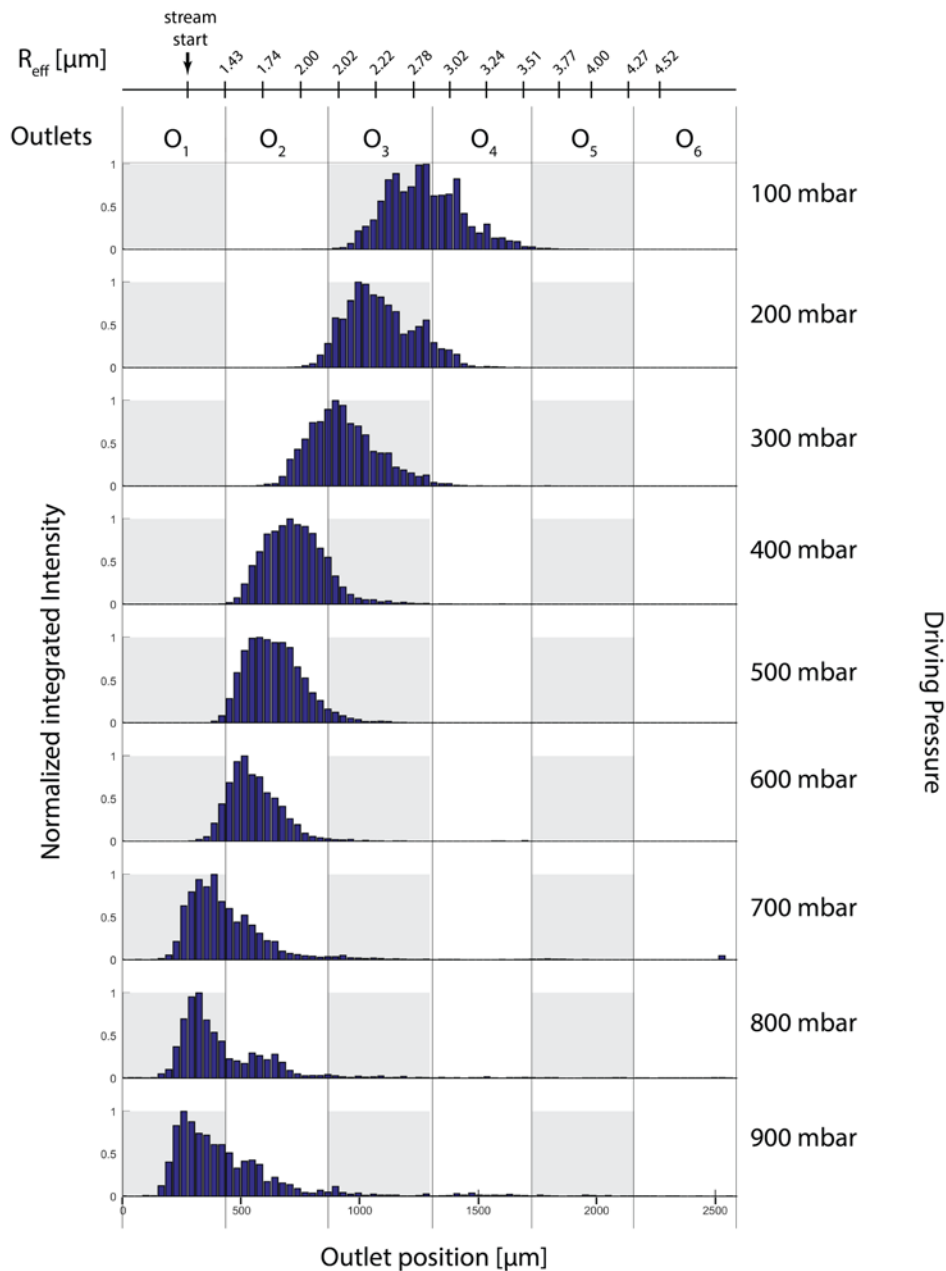


FIGURE 8.1.4: DLD Outlet distribution of driving pressures 100 mbar to 900 mbar with increments of 100 mbar. Note that various cell morphologies and not only discocytes make up the distribution. Number of cells measured for each pressure is estimated to be at least 2000-3000.

Figure 8.1.7 shows a plot of the measured cell deformation at two extreme locations (gap 10 and 22) of the outlet from fig. 8.1.7. Similar to what has been shown in fig. 8.1.6, the measured cell radius is larger for the cells that passed gap 22 (mean of $0.76 \mu\text{m}$) than gap 10 (mean of $0.76 \mu\text{m}$). The lesser mean values of the “undeformed” cells compared to that of outlet cells can be ascribed to cells being slightly deformed while flowing freely in the channels.

It can be noted that the deformation (R_{eff}/R) is generally lower for the cells further displaced (gap 22) whereas cells flowing into outlet 1 (gap 10) are deformed to a higher extent. The apparent low stiffness of the larger cells at gap 22 seems contradictory. Cells

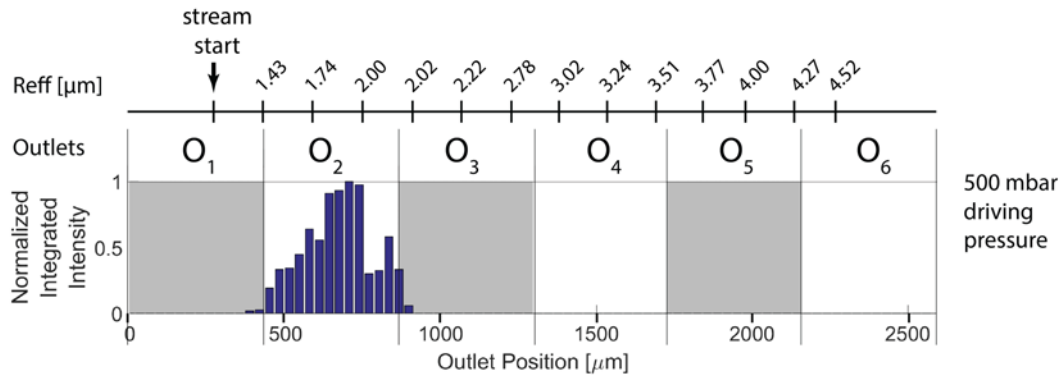


FIGURE 8.1.5: DLD Outlet distribution of a driving pressure of 500 mbar. Cells making up the distribution are mostly discocytes, see fig. 8.1.6.

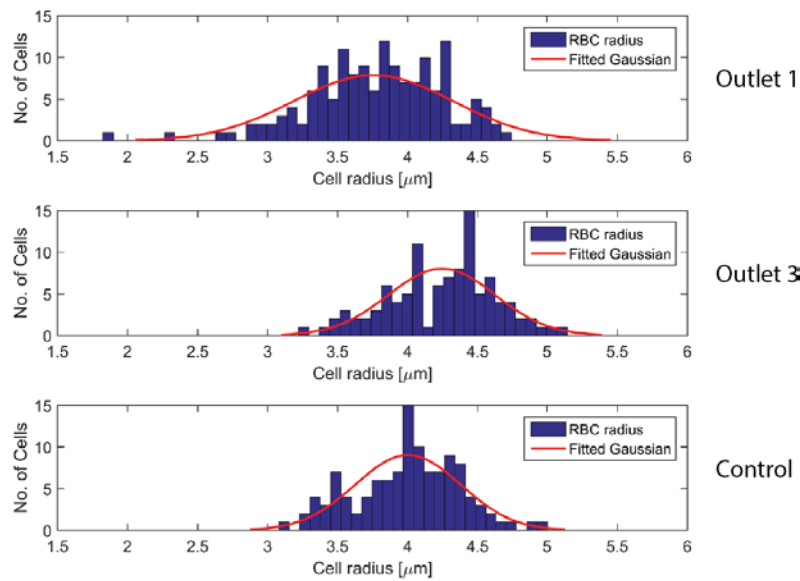


FIGURE 8.1.6: Size distributions of the separated cells of outlet 1, outlet 3 from fig. 8.1.5 and a control sample. The cell sizes were measured after 180 min of running the device and 195 min after blood collection. The cells in the control sample have been stored in a plastic tube during the DLD experiment.

with the same size but lower deformability should end up at a lower outlet position as they should deform more and thus have a smaller R_{eff} . It could be that smaller cells are generally stiffer and larger cells are generally less stiff, as cells become smaller and less deformable with aging, see chapter 5. If this effect is great enough, it would impede any cell-age fractionation by deformability that also is impacted by cell size.

By increasing the driving pressure and thus the flow rates for future experiments with a modified device design, one would possibly be able to increase the separation impact of deformability variation and lessen that of size variation. By packing the channels leading to the outlet reservoir more densely at the end of the DLD array, cell collection into distinct outlets for differing effective sizes can be achieved at higher driving pressures. This in turn depends on the optimal shear rates where separation by deformability dominates

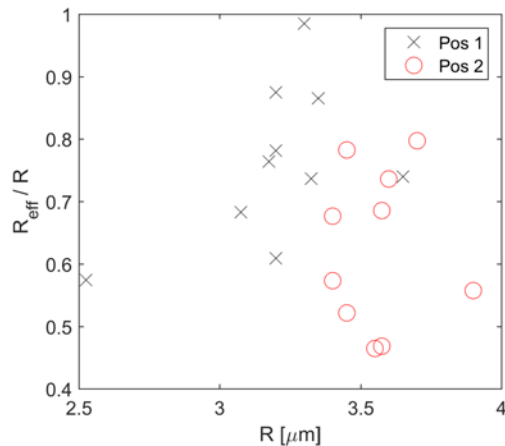


FIGURE 8.1.7: RBC Deformation to RBC size at gap 10 and 22 at section 12 near the end of the array. Outlet positions are 320 μm (outlet 1) and 704 μm (far end of outlet 2, near outlet 3) respectively. Deformation is defined as the ratio of the measured effective (deformed) radius to that of the measured radius in flow.

that of cell size. As seen in fig. 8.1.2, higher shear rates lead to a higher degree of deformation. Nonetheless, it is important that the shear rates do not exceed values which damage the cells leading to cells lyzing or impediment of the parasitic invasion process. Shear rates above 1500s^{-1} are known to lead to extensive cell damage [112]. By using the simulated shear rates, the driving pressure needed for 1500s^{-1} shear rate at the walls of the pillars in DLD can be extrapolated to around 1070 mbar.

8.1.4 Throughput

As stated by our collaborators, the RBC density has to be at least 10^4 cells per μL for proper culturing experiments. The minimum volume required to culture on a glass slide is 200 μl , meaning that at least 2 million cells have to be fractionated into each DLD outlet.

At a blood dilution of 20x and a driving pressure of 500 mbar, the shallow DLD device has a throughput of 300 000 cells/h. The 1% and 5% cell extremes as would flow into outlet 1 and 3, see fig. 8.1.4, would only be 3000 and 15000 cells/h respectively. This is too little compared to the 2 million cells needed for each sample in the *P. falciparum* culturing technique used by collaborators.

Possibly, the cell concentration could be increased with the drawback of reduced separation resolution due to particle-particle interactions.

The device throughput could be increased by parallelization or modifying the separation array design. The array could be widened and thereby lowering the hydraulic resistance. Also, more hydrodynamically designed pillars (of triangular shape) have been shown to significantly reduce the resistance and increase the throughput of the array [113].

Possibly, one could exploit the diverse dynamic flow behavior of RBCs and find where more and less deformable cells differ. If suspended in a high-viscosity medium as proposed by Henry et al. [114], one could exploit the transitions between tumbling, rolling and tank-treading motions.

8.2 Hydrodynamic Trapping

8.2.1 Fabrication

After having optimized the UV-lithography process, a variety of trap designs (see chapter 7), was fabricated and evaluated. In the first generation of traps, single-traps with narrower 1.5 μm pore widths turned out defect, with serrated edges (See example in fig. 8.2.1). This effect appeared regardless of the UV-exposure time. The 3 μm -pore traps turned out with less serration and so did the hexagonal traps (note that these had pores of 1.5 μm . Traps with cup angles of 180° had sharper corners than those of 149° and exhibited stronger defects. A too long UV-exposure time increased the serration along

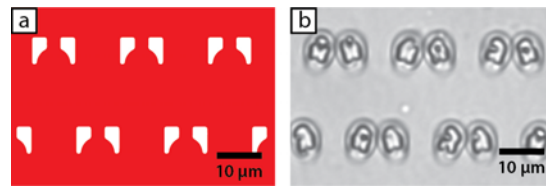


FIGURE 8.2.1: Example of edge serration by diffraction effects. (a) Trap design S3 (w of 1.5 μm and θ of 149°) (b) Trapping results of trap design S2 with first generation devices, UV exposure time of 2.1 s.

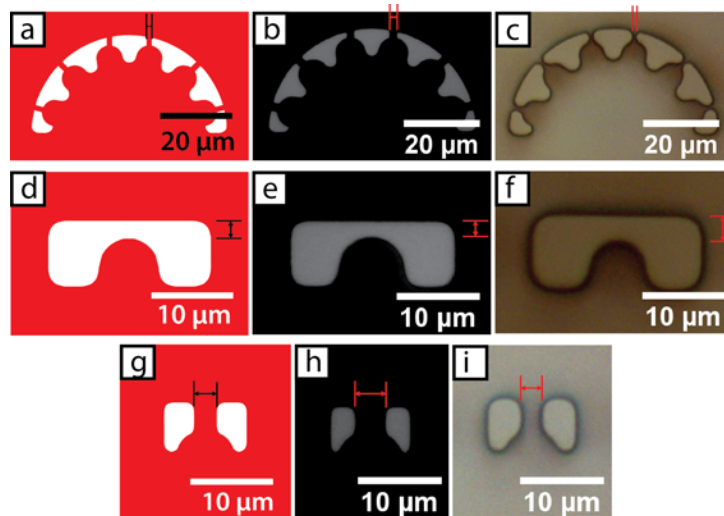


FIGURE 8.2.2: Fabrication results of second generation devices. Left: CAD design. Middle: Micrograph of the UV-lithography mask pattern. Right: Micrograph of the fabricated PDMS traps. a-c depicts hexagonal traps, d-f single no-pore s5 traps, g-i single S1 traps. Following are marked distances (approximate for micrographs): (a) 1.5 μm , (b) 2.1 μm , 1.1 (c) μm , (d) 2.2 μm , (e) 1.7 μm , (f) 3.1 μm , (g) 3 μm , (h) 3.7 μm , (i) 2.4 μm .

with too wide pores. A too short exposure dose resulted in lift-off, too narrow pores or completely obstructed pores. The optimal time differed for each trap design (3.5-4.5 s). The serration was especially apparent near corners of objects and worse for sharper corners. The serration is thought to be due to effects caused by diffraction. In high-resolution photolithography, the light has to pass small openings in the mask. Smaller features and thereby smaller openings in the mask lead to stronger diffraction-based defects.

Because of the above mentioned defects, the single-trap with 3 μm pore width and 149° cup

angle (trap S1), and the hexagonal-type trap were chosen to be included in the second generation of trap devices. Due to the higher amount of serration in narrow-pore and high angled traps, the other designs (traps S2-S4) were discarded. The fabrication process in

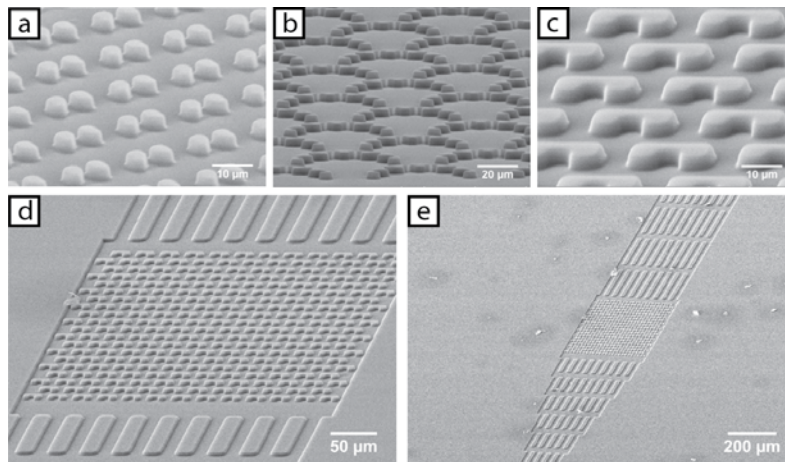


FIGURE 8.2.3: Scanning electron micrographs of trapping structures. The samples were coated with a 10 nm Platinum-Palladium (80:20) layer prior to the photos to prevent charge build-up from the electron beam. (a) Single S1 traps. (b) Hexagonal traps. (c) Single no-pore S5 traps. (d) Overview of an S5 trap array with front and back channels visible. (e) Even greater overview of the S5 trapping array. Pyramid-like channels are connected to the front-end of the traps, spreading out incoming cells evenly.

the second generation devices was altered for the prospect of less defects. A slightly denser photoresist solution was used and the baking times were reduced to 1-2 min from 8-20 min. With the higher resist density, the spin-coating speed was increased from 1000 RPM to 1800 RPM. The optimal UV-exposure time was found to be consistent with the first generation, 3.5 s. In this process, the optimal exposure time was concluded to be the same for all trap variants. The optimized protocol can be found in appendix B. This modified protocol lead to significantly improved fabrication results. Exactly why these new parameters lead to a better results is not known for certain but it could be that the photon-material-interaction and diffraction effects are different in a higher-density resist. A comparison between the mask features and the fabricated PDMS features can be seen in fig. 8.2.2 for selected traps. The final trap dimensions are slightly larger compared to the original trap dimensions in the mask. The hexagonal trap has a pore width of $\sim 1.3 \mu\text{m}$ rather than the designed $1.5 \mu\text{m}$ pore width whereas S1 has pore width of $2.3 \mu\text{m}$ instead of designed $3 \mu\text{m}$. S5 has central trap width of $3 \mu\text{m}$ rather than the designed $2 \mu\text{m}$. These results show that the fabrication could be further fine-tuned if so desired. This was not required for the proof-of-principle RBC trapping objectives of this thesis. Fig. 8.2.3 shows Scanning Electron Microscopy (SEM) photos of the traps. Even with optimized parameters, the fabricated structures won't have completely vertical walls as can be seen in the photos. The flow profile is slightly altered by the rounding, but is not thought to have large effects on the trapping efficiency.

8.2.2 Trapping

The simulation results can be seen in fig. 8.2.4. It can be noted that the hydraulic resistances and thereby volumetric flow rates through the $3 \mu\text{m}$ pores are higher than for

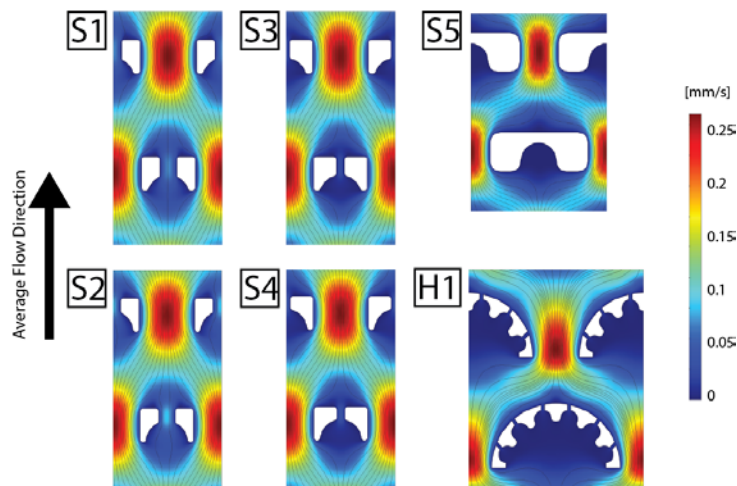


FIGURE 8.2.4: Velocity magnitude simulation with magnitude density-based streamlines of single-trap array unit cells. Applied pressure drop of $0.57 \mu\text{bar}$ across the vertical axes (equal to 100 mbar drop across the whole device). The hexagonal trap has been scaled down for comparison.

the $1.5 \mu\text{m}$ ones. Time-lapses of trapping events can be seen in fig. 8.2.5. These show how RBCs can be immobilized in various trapping structures. Only one RBCs gets immobilized in each trap. This could be due to the flexible structure inherent to the RBC, totally obstructing the flow through the pore by deformation.

In fig. 8.2.6, a plot over the trapping over time in S1, S5 and H3 arrays (second generation) can be seen. It can be observed that with the giving driving pressures, S1 fills the traps the fastest. At $t = 14 \text{ min}$, the occupancy rate (occupied traps/total no. of traps) is 85%, 0.55% and 0.27% for S1, S5 and H3 respectively. The low occupancy rate for H3 could possible be due to the narrow w (1.1 microm). By increasing w , higher occupancy rates would be expected.

The trapping is dependant on the applied inlet pressure which in turn determines the flow rate. The applied pressures have been chosen to maximize the trapping efficiencies while keeping the flow rates relatively high. The optimal pressure for trap S5 was a little lower, 30 mbar, contrasted to 60 mbar for the other trap designs. With too high pressures ($> 20 \text{ mbar}$ for the first trap generation and $> 70 \text{ mbar}$ for the second), the cells easily squeeze through the trapping pores. At very low applied pressures ($\sim 0\text{-}1 \text{ mbar}$), the cells randomly migrate out from the traps by Brownian motion.

Cells flow into the array with a slightly higher RBC concentration in the middle. This could be reduced by further optimizing the pyramid-like channel design preceding the array.

The trapping efficiency also depends on the RBC concentration. In the experiments, the concentration is low enough to be able to study single-cell trapping but not too low to reduce the trapping rate. Higher cell concentration increase the trapping rate. Cells push each other out of the streamlines and into the traps. At the same time, the total ratio of introduced cells to that of trapped cells would decrease with a higher cell concentration. As an abundance of cells are introduced to the system already, it is not of concern for the current application.

The cells seem to undergo severe deformation when being immobilized in trap with a pore,

see fig. 8.2.5 b and c. This can be contrasted to the no-pore trap where no deformation is visible, see fig. 8.2.5 a. The deformation could potentially have an effect to parasitic invasion efficiency.

When trapping cells in the parasite-infection on chip experiments, later described, it was observed that stored blood cells was considerably stiffer with very little cell deformation in the trapping process. This is consistent with other groups reporting an increased stiffness in stored blood cells, see chapter 5.

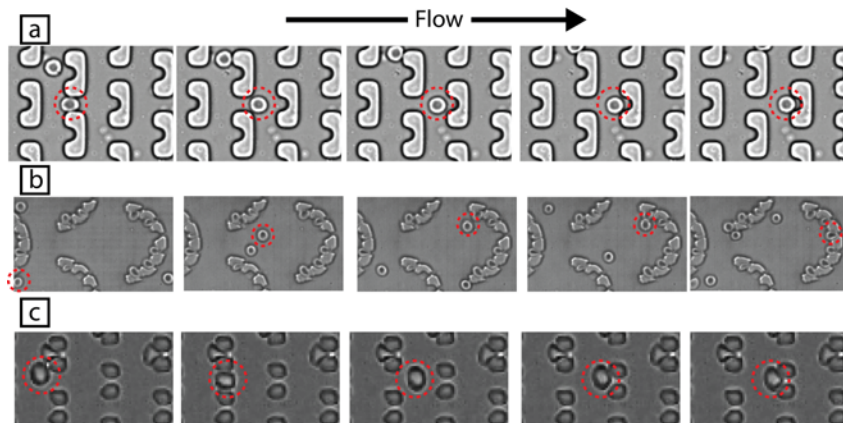


FIGURE 8.2.5: RBC trapping. (a) S5 no-pore traps. (b) Hexagonal traps (first generation). (c) S1 traps. Time steps and applied pressures are 0.03 s and 50 mbar, 1.5 s and 6 mbar, and 0.27 s and 50 mbar for a-c respectively. For clarity, red circles mark the cell being trapped.

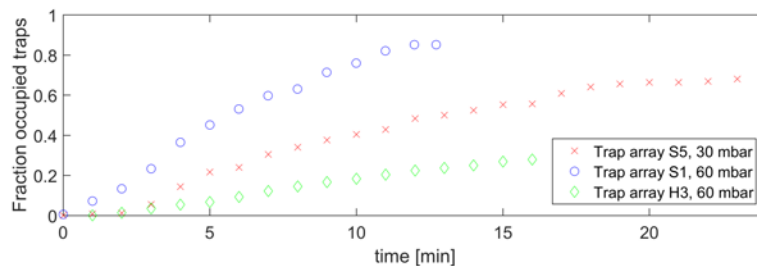


FIGURE 8.2.6: Array trapping over time for second generation trap devices.

Arc Trap

Simulation of the flow velocity in the arc trap can be seen in fig. 8.2.8 a. The channels following the traps have been designed so that their hydraulic resistance is equal.

As seen with the other trapping results, the RBC deformed significantly and covered the pore completely, even at low flow velocities. If the cell completely obstructs the trap, parasites would not flow towards the occupied trap. With this design, parasites could only possibly migrate towards an occupied trap by diffusion at very low flow rates.

While the supporting pillars were so densely packed as to be symmetrical over the traps in the arc, RBCs turned out to be trapped between them, see fig. 8.2.8 b. The pillar-pillar distances were designed to be 5.2-5.6 μm while the fabrication resulted in 3.8-4 μm in the same manner as the previously presented traps (The arc trap was included on the second-generation trap mask). As the RBCs completely obstructed the flow, increasing the distance by further optimization of the fabrication process was not pursued. Experimentation with the arc-trap was thereby discontinued.

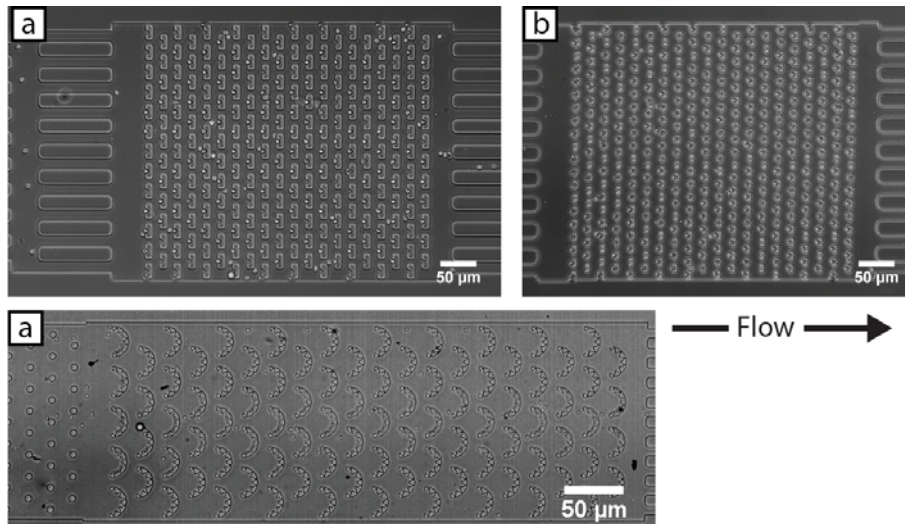


FIGURE 8.2.7: Overview micrographs of trapping. (a) $t = 24$ min for trap array S5. (b) $t = 14$ min for trap array S1. (c) $t = 16$ min for the trap array H3

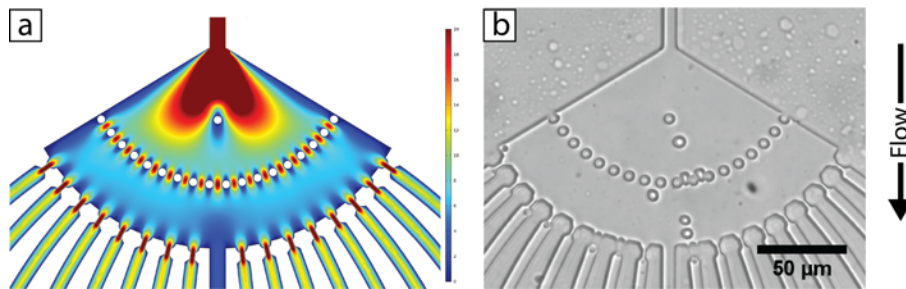


FIGURE 8.2.8: (a) Flow velocity simulation of the arc trap. Note that the flow rates into the individual trapping cups are the same. (b) RBCs flowing in the trapping area of the arc trap. Some RBCs get caught between the supporting pillars. Applied pressure drop of 20 mbar.

8.2.3 Bead interaction with trapped cells

Plastic beads with similar dimensions to the merozoite-stage parasites were used to mimic the dynamics the merozoites would have to the trapped cells. The beads, 1 μm diameter polystyrene spheres, were introduced to the array of trapped cells in the parasite inlet of the second-generation device. An excess of beads are needed to expose all trapped cells to beads as the chance of contact is quite low.

As the merozoite is non-symmetrical, see chapter 6, bead aggregates might give insight into how the rotational effect might play into the interaction. fig. 8.2.9 shows how an aggregate of 3 beads continuously rotates and hits a trapped RBC. It stays there for a while (0.8 s) and then continues past the RBC. This time can be tweaked by the applied pressure and might be enough for merozoites to attach to the cell and start invading. Interestingly, for the range of inlet pressures tested (10 - 160 mbar), beads contact with the trapped cells. At a pressure of 10 mbar, the beads that directly collide with the trapped cell stay around the cell for about 1-2 s. This can be compared to a pressure of 160 mbar where the beads stay for around 20-100 ms.

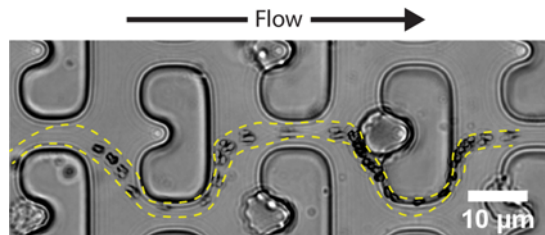


FIGURE 8.2.9: Bead aggregate interacting with a trapped cell. The image is a montage with 500 ms frame time steps. Applied pressure of 8 mbar. Dashed yellow lines added for guidance of the eye.

8.3 Parasite-infection on Chip

After having trapped cells in the array, a population of late-stage infected RBCs (iRBCs) were introduced to a separate inlet in order to infect trapped cells. The separate inlet area contained a filter obstructing the stiffer iRBCs while letting smaller merozoite-stage parasites through to the trapping array.

8.3.1 In-channel Schizont Rupturing (or lack thereof)

The schizonts first flowed into the filter area and were obstructed by the 3 μm filter (fig. 8.3.1 (a)). No in-channel rupturing was observed during several tries when waiting several hours for each experiment. Rupturing was observed in the inlet reservoir (fig. 8.3.1 (b)) where merozoite invasions of nearby cells were also occurring. The lack of rupturing was partially thought to be due to low number of schizonts present at the filter. However, it is unlikely that no schizont would rupture in a time frame longer than the synchronized rupturing time window (~ 4 h). As schizonts were rupturing in the inlet reservoir, it can be concluded that channel artefacts and most likely shape transformations were behind the inability of rupturing. It is also possible that the physical confinement itself has a role in the absence of rupturing events as it would be evolutionary advantageous to avoid rupturing in the capillaries where the supply of RBCs is low. However, possible triggers for rupture prevention in capillaries should be biochemical rather than physical deformation as the cells constantly deform when circulating in the flow larger blood vessels.

8.3.2 Echinocytosis

Many of the cells (including uninfected cells) were observed to have small thorny projections. This shape transformation is thought to have occurred after the cells entered the channel as few echinocytes were found in either of the inlet reservoirs (fig. 8.3.1 d). It is possible that the echinocytosis of the schizonts, visible in fig. 8.3.1 (a), hindered the rupturing to take place. The echinocytosis could be due to a number of factors as described in chapter 5. As the inlet reservoir possessed few echinocytes and no sign of unhealthy parasites, it is most likely that possible effects should be of the PDMS microchannels and not because of the liquid environment, temperature or gas atmosphere. It could also, although less likely, be that it is the flow shear that makes the unhealthy environment causing echinocytosis to be visible, and that cells of the inlet reservoirs are likewise affected but remain in an untriggered state. To rule this out, trial experiments where RBCs were slowly introduced into straight channels of low channel depths were conducted and

likewise, echinocytosis still occurred.

The fact that PDMS is gas-permeable would not make a big difference in the given circumstances. The PDMS layer is thick ($\sim 3-6$ mm) and there is continuous flow inside the channels to replace any medium containing a concentration increase of dissolved gases. However, if the evaporation rate through PDMS is sufficiently high at a local level, the evaporation and thereby higher medium osmolarity could induce echinocytosis. As schizonts were able to rupture in the inlet reservoir, this could not have been the deciding factor for preventing in-channel rupturing. It was noted that when switching the device substrate from PDMS to glass, the echinocytosis effect was worsened with a higher percentage of crenated cells. This further indicates that the surface effects of the PDMS and/or PLL-peg coating were likely to be behind the shape change. A longer residence time inside the channels also worsened the effect. Over time, almost all cells turned echinocytic.

It is known that echinocytic shape transformations occur near glass surfaces and between glass surfaces 0.1 mm apart. Other materials tested (vinyl, acrylate, DPX[®] and teflon) has also been reported to cause shape transformations. [111]. As the cells are confined in a channel of 4 μm , it is highly exposed to the surface and any local pH changes it musters.

8.3.3 Microorganism Contamination

During the parasite experiments, microorganism growth of both fungus and bacteria inside the channels was observed, see fig. 8.3.1 (c). The nutrient dense medium and the in-channel temperature (37°C) makes the environment hospitable for microorganisms. To prevent the contamination from reoccurring in later experiments, an ethanol-washing protocol of the channels was adopted before the introduction of any cell sample.

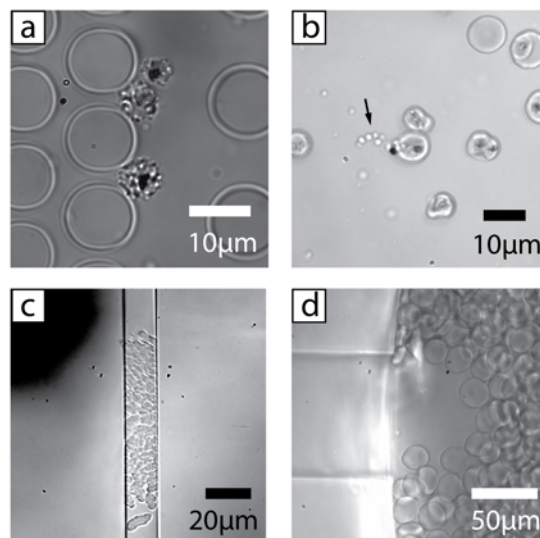


FIGURE 8.3.1: (a) Schizonts obstructed by the filter, where all visible three cells are severely echinocytic. Schizonts can be distinguished from uninfected cells by their black pigment. (b) Parasites in the inlet reservoir, unaffected by any shape transformation. Arrow denotes freely diffusing merozoites. (c) Channel obstructed by fungus growth. (d) Inlet reservoir of uninfected RBCs with no indication of echinocytosis.

Chapter 9

Conclusion

This thesis investigated the prospects of studying a cell age-coupled preferential invasion of *P. Falciparum* of RBCs by fractionating RBC populations by deformability using Deterministic Lateral Displacement. Increased cell deformation in DLD was observed with higher shear rates at higher applied device pressures. The DLD outlet distribution also shifted towards less displacement when the applied pressure was increased confirming the reduction of the effective size by deformation. However, the size variation in the sample was significant and impeded separation by deformability at a high driving pressure of 500 mbar. This driving pressure was chosen as it allowed collection and property comparison of the extreme population fractions (most and least deformable cells).

At this pressure, the displacing cells were generally larger and more deformable whereas the less displacing cells were smaller and less deformable. To reduce the effect of size, the driving pressure could be further increased although a redesign of the outlet positions at the end of the array is needed.

Hydrodynamic trapping arrays incorporating high-resolution cell trapping structures were designed, simulated and fabricated to study on-chip invasion of trapped RBCs.

RBCs were trapped in various trap designs with high trap occupancy rates (up to 85% over the span of 14 minutes) and contact of introduced beads mimicking parasites to trapped cells was confirmed.

Abnormal shape transformation of RBCs into crenated echinocytes was observed when introduced into 4 μm shallow PDMS channels. This is concluded to be due to the “glass effect” where locally increased pH levels near artificial surfaces induce crenated shape changes of RBCs. The shape transformation changes both deformability and size of the RBCs which affects the fractionation in DLD. It is however possible that the deformability-differences in subpopulations of differing cell ages remain with transformed shape and can still be separated by DLD.

In-channel parasitic behavior was also investigated. An in-channel incapacity of infected RBCs to rupture was discovered. This is thought to be related to the observed shape transformation.

9.1 Outlook

The work started in this thesis shows future potential and continued research is proposed. The separation of young and old RBCs by deformability could yield improved results compared to separating cell ages by density. The further investigation of a preferential invasion of deformability-separated cells could therefore be highly rewarding.

It is advised that the deformability and age variations in DLD-separated samples are benchmarked against alternative techniques for a more thorough understanding of the RBC behavior in DLD.

With shallow-channel DLD devices as presented in this thesis, the throughput is too low

for post-separation culturing in conventional manners. Boosting the cell throughput by device redesign should be considered. Alternatively, other culturing methods requiring less blood sample could be utilized. On-chip invasion is a convenient method with no sample loss otherwise found in conventional techniques.

Artefacts created by channel confinement could possibly be reduced by varying the channel material or altering the channel surface coating.

The hydrodynamic trapping arrays for immobilizing RBCs could also be adopted for other purposes. The arrays allow for exposing cells (healthy or diseased) to various pharmaceutical or biochemical substances.

Appendix A: Blood sample extraction handling and preparation

1. First clean the puncture site (side of a finger) with ethanol to remove any dust or bacteria.
2. Puncture the site with a blood prick and gently squeeze around the site to extract more blood from the wound. Avoid squeezing too hard as it can cause interstitial tissue fluid to dilute the droplet.
3. Wipe the first blood drop away as it could be contaminated with microorganisms, tissue fluid or skin debris. It also contains the platelet plug. Without washing away the platelet plug, the blood flow may stop prior to completion.
4. Aspirate the desired blood volume (20-50 μL) to a tube prefilled with an anticoagulant. Here either of two anticoagulants were used ethylenediaminetetraacetic acid (EDTA), diluted in autoMACS[®] (Miltenyi Biotec, Lund, Sweden) or anticoagulant or citrate phosphate dextrose adenine (CPDA) which should be mixed with blood at a volume ratio of 12.2
5. Mix by turning the sample upside down 10 times
6. Centrifuge the solution in a centrifuge at 400 RCF (relative centrifugal force) for 2 minutes (RCF over 400 g can lead to cells lysing).
7. Replace the supernatant with buffer, either autoMACS[®], phosphate buffer solution (PBS) or the culture medium.

Appendix B: UV Lithography Protocol

for SU-8 2005 4 μ m deep features

#1 Substrate Pre-treatment - Omnicoat (Adhesive Layer)

1. Spin coating
 - Static Dispense with approximately 1ml of Omnicoat per inch of wafer diameter.
 - Spreading Spin at 500 RPM for 5 sec with acceleration of 100 RPM/s.
 - Main Spin at 3000 rpm for 30 sec with acceleration of 300 rpm/s.
2. Baking at 200° C hotplate for 1 min; allow substrate to cool to room temperature

#2 SU-8 Spin Coating

1. Static Dispense with approximately 1 ml of SU-8 per inch of wafer diameter.
2. Spreading spin at 500 rpm for 5 sec with an acceleration of 100 RPM/s.
3. Main spin at 2000 RPM for 30 sec with acceleration of 300 RPM/s.

#3 Soft Baking

1. Pre-baking on hot-plate for 1 minute at 65° C
2. Soft-baking on hot-plate for 2 minutes at 95° C
3. (Edge Bead Removal) (Both normal & coffee ring effect-derived edge bead) – Swipe the wafer edges off with acetone.

#4 UV Treatment & Development

1. UV Exposure (near UV [350-400nm]) 3.4 seconds exposure dose with a constant intensity of 20mW/cm² using vacuum contact mode with a mask aligner (Karl Sss MJB3 and MJB4, Mnich Germany)
2. Post-Exposure Baking
 - (a) Pre-baking on hot-plate for 1 minute at 65° C
 - (b) Post-Exposure baking for 2.5 minutes at 95° C
 - (c) Cool down to room temperature for 4-5 min.
3. Development with mr-Dev 600 (Microresist Technology) for 1 minute.
4. Rinsing with mr-Dev 600 & Isoproponal and then drying with nitrogen gas.
5. Hard Baking for 2h at 200° C in a convection oven

#4 Anti-adhesion Treatment

1. Insert the wafer into the glove box (Nitrogen Atmosphere)
2. Place the wafer inside a glass-container.
3. Inject the anti-adhesion agent 1H,1H,2H,2H-perfluorooctyltrichlorosilane (ABC R GmbH % Co. KG, Karlsruhe, Germany) into the container.
4. Set the heating to about 200 °C (boiling temperature is 180°C) and put seal the glass container.
5. Let the wafer sit inside the container for 4 hours.

Appendix C: Soft lithography protocol

PDMS coated glass slide

1. Cleaning of the glass slide (76 x 26 mm) with IPA (Iso-Propanyl Alcohol) and Nitrogen gas pistol
2. Poly-Di-Methyl-Siloxane (PDMS), SYLGARD[®] 184 Silicone Elastomer Kit, Dow Corning) Deposition onto the glass slide($\sim 2\text{g}$)!
3. Spin coating at 3000 RPM for 30 seconds
4. 1-48 hours at 80°

PDMS device

1. Thorough mixing PDMS and cross-linking agent, to a ratio of 8:1 (standard protocol is 10:1).
2. Degassing in a vacuum desiccator for 30 min.
3. Pouring of the PDMS solution onto the patterned silicon wafer.
4. Baking in oven for 1 hour at 80 °. Make sure to keep the substrate level inside the oven to avoid any unevenness.
5. Removal of excess PDMS and storage on a cleaned glass slide
6. Reservoir Hole Punching with a 2 mm hole-puncher for non-sample holes. For the sample hole, a 3 mm hole-puncher is used to make room for the magnetic stirring bar.
7. Pre-Plasma Cleaning with Scotch Tape (3M)
8. Plasma Oxidation for 30s (Plasma Preen II-862, Plasmatic Systems Inc., North Brunswick, NJ, USA)
9. Careful bonding of the PDMS slab to a PDMS coated glass slide.
10. Channel wetting with 0.2% PLL-g-PEG(poly(L-lysine)-graft-poly(ethylene glycol)) (SuSoS AG, Dübendorf, Switzerland)
11. Gluing of silicone tube reservoirs onto punched inlet and outlet holes with silicone adhesive A07 (Wacker Chemie AG, München, Germany). The tubes are cleaned with ultrasonication in ethanol for 5 minutes and then in milli-Q water for 5 minutes.
12. Device ready to use.

Appendix D: DLD array characteristics

TABLE 9.1.1: Section-by-section parameter values of DLD Device. $G = 12\mu\text{m}$, $\lambda = 32\mu\text{m}$, $D_{post} = 20\mu\text{m}$

Section	$\Delta\lambda$ [μm]	N	Number of Rows	R_c [μm]	Disp. [μm]
1	0.8	36.71	200	1.43	160
2	1.2	26.67	130	1.74	316
3	1.6	20	100	2.00	476
4	2	16	80	2.02	636
5	2.6	12.31	60	2.22	792
6	3.2	10	50	2.78	952
7	3.8	8.42	40	3.02	1104
8	4.4	7.27	35	3.24	1258
9	5.2	6.15	30	3.51	1414
10	6	5.33	24	3.77	1564
11	6.8	4.71	20	4.00	1700
12	7.8	4.1	20	4.27	1856
13	8.8	3.64	15	4.52	1988

Bibliography

- [1] World Health Organization. World malaria report 2015. Technical report, 2015.
- [2] Douglas H Kerlin and Michelle L Gatton. Preferential invasion by plasmodium merozoites and the self-regulation of parasite burden. *PloS one*, 8(2):e57434, 2013.
- [3] G Pasvol, DJ Weatherall, and RJM Wilson. The increased susceptibility of young red cells to invasion by the malarial parasite plasmodium falciparum. *British journal of haematology*, 45(2):285–295, 1980.
- [4] Robert Hegner et al. Relative frequency of ring-stage plasmodia in reticulocytes and mature erythrocytes in man and monkey. *American Journal of Hygiene*, 27(3):690–718, 1938.
- [5] Richard E Waugh, Mohandas Narla, Carl W Jackson, Thomas J Mueller, Takashige Suzuki, and George L Dale. Rheologic properties of senescent erythrocytes: loss of surface area and volume with red blood cell age. *Blood*, 79(5):1351–1358, 1992.
- [6] Robert S Franco, M Estela Puchulu-Campanella, Latorya A Barber, Mary B Palascak, Clinton H Joiner, Philip S Low, and Robert M Cohen. Changes in the properties of normal human red blood cells during in vivo aging. *American journal of hematology*, 88(1):44–51, 2013.
- [7] SP Sutera, RA Gardner, CW Boylan, GL Carroll, KC Chang, JS Marvel, C Kilo, B Gonen, and JR Williamson. Age-related changes in deformability of human erythrocytes. *Blood*, 65(2):275–282, 1985.
- [8] JGG Dobbe, GJ Streekstra, MR Hardeman, C Ince, and CA Grimbergen. Measurement of the distribution of red blood cell deformability using an automated rheoscope. *Cytometry*, 50(6):313–325, 2002.
- [9] Maria Fornal, Małgorzata Lekka, Grażyna Pyka-Fościk, Kateryna Lebed, Tomasz Grodzicki, Barbara Wizner, and Jan Styczeń. Erythrocyte stiffness in diabetes mellitus studied with atomic force microscope. *Clinical hemorheology and microcirculation*, 35(1, 2):273–276, 2006.
- [10] Shu Chien, Shunichi Usami, and John F Bertles. Abnormal rheology of oxygenated blood in sickle cell anemia. *Journal of Clinical Investigation*, 49(4):623, 1970.
- [11] YongKeun Park, Monica Diez-Silva, Dan Fu, Gabriel Popescu, Wonshik Choi, Ishan Barman, Subra Suresh, and Michael S Feld. Static and dynamic light scattering of healthy and malaria-parasite invaded red blood cells. *Journal of biomedical optics*, 15(2):020506–020506, 2010.
- [12] Herbert J Meiselman, Evan A Evans, and Robert M Hochmuth. Membrane mechanical properties of atp-depleted human erythrocytes. *Blood*, 52(3):499–504, 1978.
- [13] Marcel Bessis, Narla Mohandas, and Claude Feo. Automated ektacytometry: a new method of measuring red cell deformability and red cell indices. *Blood cells*, 6(3):315–327, 1979.

- [14] Manfred Radmacher. Measuring the elastic properties of biological samples with the afm. *IEEE Engineering in Medicine and Biology Magazine*, 16(2):47–57, 1997.
- [15] Robert M Hochmuth. Micropipette aspiration of living cells. *Journal of biomechanics*, 33(1):15–22, 2000.
- [16] Andreas R Bausch, Winfried Möller, and Erich Sackmann. Measurement of local viscoelasticity and forces in living cells by magnetic tweezers. *Biophysical journal*, 76(1):573–579, 1999.
- [17] Olivier Thoumine and Albrecht Ott. Time scale dependent viscoelastic and contractile regimes in fibroblasts probed by microplate manipulation. *Journal of cell science*, 110(17):2109–2116, 1997.
- [18] Jochen Guck, Revathi Ananthakrishnan, Hamid Mahmood, Tess J Moon, C Casey Cunningham, and Josef Käs. The optical stretcher: a novel laser tool to micromanipulate cells. *Biophysical journal*, 81(2):767–784, 2001.
- [19] Han Wei Hou, Ali Asgar S Bhagat, Alvin Guo Lin Chong, Pan Mao, Kevin Shyong Wei Tan, Jongyoon Han, and Chwee Teck Lim. Deformability based cell margination—a simple microfluidic design for malaria-infected erythrocyte separation. *Lab on a Chip*, 10(19):2605–2613, 2010.
- [20] Soojung Claire Hur, Nicole K Henderson-MacLennan, Edward RB McCabe, and Dino Di Carlo. Deformability-based cell classification and enrichment using inertial microfluidics. *Lab on a Chip*, 11(5):912–920, 2011.
- [21] Hansen Bow, Igor V Pivkin, Monica Diez-Silva, Stephen J Goldfless, Ming Dao, Jacquin C Niles, Subra Suresh, and Jongyoon Han. A microfabricated deformability-based flow cytometer with application to malaria. *Lab on a Chip*, 11(6):1065–1073, 2011.
- [22] Jason P Beech, Stefan H Holm, Karl Adolfsson, and Jonas O Tegenfeldt. Sorting cells by size, shape and deformability. *Lab on a Chip*, 12(6):1048–1051, 2012.
- [23] Quan Guo, Simon P Duffy, Kerryn Matthews, Xiaoyan Deng, Aline T Santoso, Emel Islamzada, and Hongshen Ma. Deformability based sorting of red blood cells improves diagnostic sensitivity for malaria caused by plasmodium falciparum. *Lab on a Chip*, 16(4):645–654, 2016.
- [24] Lotien Richard Huang, Edward C Cox, Robert H Austin, and James C Sturm. Continuous particle separation through deterministic lateral displacement. *Science*, 304(5673):987–990, 2004.
- [25] John A Davis, David W Inglis, Keith J Morton, David A Lawrence, Lotien R Huang, Stephen Y Chou, James C Sturm, and Robert H Austin. Deterministic hydrodynamics: taking blood apart. *Proceedings of the National Academy of Sciences*, 103(40):14779–14784, 2006.
- [26] Zongbin Liu, Fei Huang, Jinghui Du, Weiliang Shu, Hongtao Feng, Xiaoping Xu, and Yan Chen. Rapid isolation of cancer cells using microfluidic deterministic lateral displacement structure. *Biomicrofluidics*, 7(1):011801, 2013.

- [27] Stefan H Holm, Jason P Beech, Michael P Barrett, and Jonas O Tegenfeldt. Separation of parasites from human blood using deterministic lateral displacement. *Lab on a Chip*, 11(7):1326–1332, 2011.
- [28] David Holmes, Graeme Whyte, Joe Bailey, Nuria Vergara-Irigaray, Andrew Ekpenyong, Jochen Guck, and Tom Duke. Separation of blood cells with differing deformability using deterministic lateral displacement. *Interface Focus*, 4(6):20140011, 2014.
- [29] Raymond Quek, Duc Vinh Le, and K-H Chiam. Separation of deformable particles in deterministic lateral displacement devices. *Physical Review E*, 83(5):056301, 2011.
- [30] Timm Krüger, David Holmes, and Peter V Coveney. Deformability-based red blood cell separation in deterministic lateral displacement devices—a simulation study. *Biomicrofluidics*, 8(5):054114, 2014.
- [31] Zunmin Zhang, Ewan Henry, Gerhard Gompper, and Dmitry A Fedosov. Behavior of rigid and deformable particles in deterministic lateral displacement devices with different post shapes. *The Journal of chemical physics*, 143(24):243145, 2015.
- [32] Aaron R Wheeler, William R Thronset, Rebecca J Whelan, Andrew M Leach, Richard N Zare, Yish Hann Liao, Kevin Farrell, Ian D Manger, and Antoine Dardon. Microfluidic device for single-cell analysis. *Analytical chemistry*, 75(14):3581–3586, 2003.
- [33] Dino Di Carlo, Nima Aghdam, and Luke P Lee. Single-cell enzyme concentrations, kinetics, and inhibition analysis using high-density hydrodynamic cell isolation arrays. *Analytical chemistry*, 78(14):4925–4930, 2006.
- [34] Alison M Skelley, Oktay Kirak, Heikyung Suh, Rudolf Jaenisch, and Joel Voldman. Microfluidic control of cell pairing and fusion. *Nature methods*, 6(2):147–152, 2009.
- [35] Eric Brouzes, Martina Medkova, Neal Savenelli, Dave Marran, Mariusz Twardowski, J Brian Hutchison, Jonathan M Rothberg, Darren R Link, Norbert Perrimon, and Michael L Samuels. Droplet microfluidic technology for single-cell high-throughput screening. *Proceedings of the National Academy of Sciences*, 106(34):14195–14200, 2009.
- [36] Albert Folch. *Introduction to bioMEMS*. CRC Press, 2016.
- [37] Henrik Bruus. *Theoretical microfluidics*. 2008.
- [38] Martin Heller and Henrik Bruus. A theoretical analysis of the resolution due to diffusion and size dispersion of particles in deterministic lateral displacement devices. *Journal of Micromechanics and Microengineering*, 18(7):075030, 2008.
- [39] Brian R Long, Martin Heller, Jason P Beech, Heiner Linke, Henrik Bruus, and Jonas O Tegenfeldt. Multidirectional sorting modes in deterministic lateral displacement devices. *Physical Review E*, 78(4):046304, 2008.
- [40] Kevin Loutherbach, Joseph D’Silva, Liyu Liu, Amy Wu, Robert H Austin, and James C Sturm. Deterministic separation of cancer cells from blood at 10 ml/min. *AIP advances*, 2(4):042107, 2012.

- [41] John Alan Davis. *Microfluidic separation of blood components through deterministic lateral displacement*. PhD thesis, Princeton University, 2008.
- [42] Jason Beech. *Microfluidics Separation and Analysis of Biological Particles*. Lund University, 2011.
- [43] J McGrath, M Jimenez, and H Bridle. Deterministic lateral displacement for particle separation: a review. *Lab on a Chip*, 14(21):4139–4158, 2014.
- [44] Timm Krüger, David Holmes, Peter V Coveney, et al. Deformability of red blood cells affects their velocity in deterministic lateral displacement devices. 2014.
- [45] Dmitry A Fedosov, Bruce Caswell, and George Em Karniadakis. A multiscale red blood cell model with accurate mechanics, rheology, and dynamics. *Biophysical journal*, 98(10):2215–2225, 2010.
- [46] Albert Folch. *Introduction to bioMEMS*. CRC Press, 2016.
- [47] Wei-Heong Tan and Shoji Takeuchi. A trap-and-release integrated microfluidic system for dynamic microarray applications. *Proceedings of the National Academy of Sciences*, 104(4):1146–1151, 2007.
- [48] Stefan Kobel, Ana Valero, Jonas Latt, Philippe Renaud, and Matthias Lutolf. Optimization of microfluidic single cell trapping for long-term on-chip culture. *Lab on a Chip*, 10(7):857–863, 2010.
- [49] J Patrick Shelby, John White, Karthikeyan Ganesan, Pradipsinh K Rathod, and Daniel T Chiu. A microfluidic model for single-cell capillary obstruction by plasmodium falciparum-infected erythrocytes. *Proceedings of the National Academy of Sciences*, 100(25):14618–14622, 2003.
- [50] Robert I Weed, Claude F Reed, and George Berg. Is hemoglobin an essential structural component of human erythrocyte membranes? *Journal of Clinical Investigation*, 42(4):581, 1963.
- [51] Robert S Franco. Measurement of red cell lifespan and aging. *Transfusion Medicine and Hemotherapy*, 39(5):302–307, 2012.
- [52] Hans U Lutz and Anna Bogdanova. Mechanisms tagging senescent red blood cells for clearance in healthy humans. *Regulation of red cell life-span, erythropoiesis, senescence and clearance*, page 45, 2007.
- [53] Robert I Weed. The importance of erythrocyte deformability. *The American journal of medicine*, 49(2):147–150, 1970.
- [54] Joel Anne Chasis and Stephen B Shoet. Red cell biochemical anatomy and membrane properties. *Annual review of physiology*, 49(1):237–248, 1987.
- [55] Shu Chien. Red cell deformability and its relevance to blood flow. *Annual review of physiology*, 49(1):177–192, 1987.
- [56] Giovanna Tomaiuolo. Biomechanical properties of red blood cells in health and disease towards microfluidics. *Biomicrofluidics*, 8(5):051501, 2014.

- [57] YongKeun Park, Catherine A Best, Tatiana Kuriabova, Mark L Henle, Michael S Feld, Alex J Levine, and Gabriel Popescu. Measurement of the nonlinear elasticity of red blood cell membranes. *Physical Review E*, 83(5):051925, 2011.
- [58] SJ Singer and Garth L Nicolson. The fluid mosaic model of the structure of cell membranes. *Membranes and Viruses in Immunopathology; Day, SB, Good, RA, Eds*, pages 7–47, 1972.
- [59] RICHARD E Waugh. Surface viscosity measurements from large bilayer vesicle tether formation. ii. experiments. *Biophysical journal*, 38(1):29, 1982.
- [60] Youngchan Kim, Kyoo Hyun Kim, and YongKeun Park. *Measurement techniques for red blood cell deformability: recent advances*. INTECH Open Access Publisher, 2012.
- [61] R Waugh and EA Evans. Thermoelasticity of red blood cell membrane. *Biophysical journal*, 26(1):115, 1979.
- [62] Evan A Evans and Paul L La Celle. Intrinsic material properties of the erythrocyte membrane indicated by mechanical analysis of deformation. *Blood*, 45(1):29–43, 1975.
- [63] Marina Puig-de Morales-Marinkovic, Kevin T Turner, James P Butler, Jeffrey J Fredberg, and Subra Suresh. Viscoelasticity of the human red blood cell. *American Journal of Physiology-Cell Physiology*, 293(2):C597–C605, 2007.
- [64] Guillaume Lenormand, Sylvie Hénon, Alain Richert, Jacqueline Siméon, and François Gallet. Direct measurement of the area expansion and shear moduli of the human red blood cell membrane skeleton. *Biophysical Journal*, 81(1):43–56, 2001.
- [65] EVAN A Evans. Bending elastic modulus of red blood cell membrane derived from buckling instability in micropipet aspiration tests. *Biophysical Journal*, 43(1):27, 1983.
- [66] NZ Piety, SC Gifford, X Yang, and SS Shevkopyas. Quantifying morphological heterogeneity: a study of more than 1 000 000 individual stored red blood cells. *Vox sanguinis*, 109(3):221–230, 2015.
- [67] WCO Tsang. *The size and shape of human red blood cells*. PhD thesis, MS Thesis. University of California San Diego, La Jolla, CA, 1975.
- [68] Evan Evans and Yuan-Cheng Fung. Improved measurements of the erythrocyte geometry. *Microvascular research*, 4(4):335–347, 1972.
- [69] Gerald Lim HW, Michael Wortis, and Ranjan Mukhopadhyay. Stomatocyte–discocyte–echinocyte sequence of the human red blood cell: Evidence for the bilayer–couple hypothesis from membrane mechanics. *Proceedings of the National Academy of Sciences*, 99(26):16766–16769, 2002.
- [70] Michael P Sheetz and SJ Singer. Biological membranes as bilayer couples. a molecular mechanism of drug-erythrocyte interactions. *Proceedings of the National Academy of Sciences*, 71(11):4457–4461, 1974.

- [71] Megha Singh and JF Stoltz. Influence of temperature variation from 5 c to 37 c on aggregation and deformability of erythrocytes. *Clinical hemorheology and microcirculation*, 26(1):1–7, 2002.
- [72] Makoto Nakao, Toshiko Nakao, and Saburo Yamazoe. Adenosine triphosphate and maintenance of shape of the human red cells. 1960.
- [73] Robert I Weed, Paul L LaCelle, and Edward W Merrill. Metabolic dependence of red cell deformability. *Journal of Clinical Investigation*, 48(5):795, 1969.
- [74] Jeongho Kim, HoYoon Lee, and Sehyun Shin. Advances in the measurement of red blood cell deformability: A brief review. *Journal of Cellular Biotechnology*, 1(1):63–79, 2015.
- [75] Melek Bor-Kucukatay, Rosalinda B Wenby, Herbert J Meiselman, and Oguz K Baskurt. Effects of nitric oxide on red blood cell deformability. *American Journal of Physiology-Heart and Circulatory Physiology*, 284(5):H1577–H1584, 2003.
- [76] R Khecuriani, G Lomsadze, M Arabuli, and T Sanikidze. Deformability of red blood cells and human aging. *Georgian Med News*, 182:42–46, 2010.
- [77] MV Kameneva, KO Garrett, MJ Watach, and HS Borovetz. Red blood cell aging and risk of cardiovascular diseases. *Clinical hemorheology and microcirculation*, 18(1):67–74, 1998.
- [78] UJ Kirkpatrick, RA Adams, A Lardi, and CN McCollum. Rheological properties and function of blood cells in stored bank blood and salvaged blood. *British journal of haematology*, 101(2):364–368, 1998.
- [79] PL Celle. Alteration of deformability of the erythrocyte membrane in stored blood. *Transfusion*, 9(5):238–245, 1969.
- [80] RR Huruta, ML Barjas-Castro, STO Saad, FF Costa, A Fontes, LC Barbosa, and CL Cesar. Mechanical properties of stored red blood cells using optical tweezers. *Blood*, 92(8):2975–2977, 1998.
- [81] P Izzo, A Manicone, A Spagnuolo, VM Lauti, A Di Pasquale, and D Di Monte. Erythrocytes stored in cpd sag-mannitol: evaluation of their deformability. *Clinical hemorheology and microcirculation*, 21(3, 4):335–339, 1999.
- [82] Ameya Sinha, Trang TT Chu, Ming Dao, and Rajesh Chandramohanadas. Single-cell evaluation of red blood cell bio-mechanical and nano-structural alterations upon chemically induced oxidative stress. *Scientific reports*, 5, 2015.
- [83] Joy Mohanty, Enika Nagababu, and Joseph M Rifkind. Red blood cell oxidative stress impairs oxygen delivery and induces red blood cell aging. *Frontiers in physiology*, 5:84, 2014.
- [84] Frans LA Willekens, Jan M Werre, Yvonne AM Groenen-Döpp, Bregt Roerdinkholder-Stoelwinder, Ben De Pauw, and Giel JCGM Bosman. Erythrocyte vesiculation: a self-protective mechanism? *British journal of haematology*, 141(4):549–556, 2008.

- [85] Gregorsz Bartosz. Erythrocyte aging: physical and chemical membrane changes. *Gerontology*, 37(1-3):33–67, 1991.
- [86] FH Bosch, JM Werre, B Roerdinkholder-Stoelwinder, TH Huls, FL Willekens, and MR Halie. Characteristics of red blood cell populations fractionated with a combination of counterflow centrifugation and percoll separation. *Blood*, 79(1):254–260, 1992.
- [87] AR Williams and DR Morris. The internal viscosity of the human erythrocyte may determine its lifespan in vivo. *Scandinavian journal of haematology*, 24(1):57–62, 1980.
- [88] FLA Willekens, FH Bosch, B Roerdinkholder-Stoelwinder, YAM Groenen-Döpp, and JM Werre. Quantification of loss of haemoglobin components from the circulating red blood cell in vivo. *European journal of haematology*, 58(4):246–250, 1997.
- [89] Hiroshi Noguchi and Gerhard Gompper. Shape transitions of fluid vesicles and red blood cells in capillary flows. *Proceedings of the National Academy of Sciences of the United States of America*, 102(40):14159–14164, 2005.
- [90] Kosuke Tsukada, Eiichi Sekizuka, Chikara Oshio, and Haruyuki Minamitani. Direct measurement of erythrocyte deformability in diabetes mellitus with a transparent microchannel capillary model and high-speed video camera system. *Microvascular research*, 61(3):231–239, 2001.
- [91] Jules Dupire, Marius Socol, and Annie Viallat. Full dynamics of a red blood cell in shear flow. *Proceedings of the National Academy of Sciences*, 109(51):20808–20813, 2012.
- [92] Thomas M Fischer. Tank-tread frequency of the red cell membrane: dependence on the viscosity of the suspending medium. *Biophysical journal*, 93(7):2553–2561, 2007.
- [93] Alireza ZK Yazdani and Prosenjit Bagchi. Phase diagram and breathing dynamics of a single red blood cell and a biconcave capsule in dilute shear flow. *Physical Review E*, 84(2):026314, 2011.
- [94] Manouk Abkarian, Magalie Faivre, and Annie Viallat. Swinging of red blood cells under shear flow. *Physical review letters*, 98(18):188302, 2007.
- [95] Adrian VS Hill. Vaccines against malaria. *Philosophical Transactions of the Royal Society B: Biological Sciences*, 366(1579):2806–2814, 2011.
- [96] Paul R Gilson and Brendan S Crabb. Morphology and kinetics of the three distinct phases of red blood cell invasion by plasmodium falciparum merozoites. *International journal for parasitology*, 39(1):91–96, 2009.
- [97] Michelle J Boyle, Danny W Wilson, and James G Beeson. New approaches to studying plasmodium falciparum merozoite invasion and insights into invasion biology. *International journal for parasitology*, 43(1):1–10, 2013.

- [98] Aidan J O'Donnell, Petra Schneider, Harriet G McWatters, and Sarah E Reece. Fitness costs of disrupting circadian rhythms in malaria parasites. *Proceedings of the Royal Society of London B: Biological Sciences*, page rspb20102457, 2011.
- [99] Michelle J Boyle, Danny W Wilson, Jack S Richards, David T Riglar, Kevin KA Tetteh, David J Conway, Stuart A Ralph, Jake Baum, and James G Beeson. Isolation of viable plasmodium falciparum merozoites to define erythrocyte invasion events and advance vaccine and drug development. *Proceedings of the National Academy of Sciences*, 107(32):14378–14383, 2010.
- [100] Tenghu Wu and James J Feng. Simulation of malaria-infected red blood cells in microfluidic channels: Passage and blockage. *Biomicrofluidics*, 7(4):044115, 2013.
- [101] John EK Mrema, Susan G Langreth, Robert C Jost, Karl H Rieckmann, and Hans-G Heidrich. Plasmodium falciparum: isolation and purification of spontaneously released merozoites by nylon membrane sieves. *Experimental parasitology*, 54(3):285–295, 1982.
- [102] Alex J Crick, Michel Theron, Teresa Tiffert, Virgilio L Lew, Pietro Cicuta, and Julian C Rayner. Quantitation of malaria parasite-erythrocyte cell-cell interactions using optical tweezers. *Biophysical journal*, 107(4):846–853, 2014.
- [103] David W Inglis. Efficient microfluidic particle separation arrays. *Applied Physics Letters*, 94(1):013510, 2009.
- [104] Kjell S Sakariassen, Lars Orning, and Vincent T Turitto. The impact of blood shear rate on arterial thrombus formation. *Future Science OA*, 1(4), 2015.
- [105] Quan Guo, Sarah J Reiling, Petra Rohrbach, and Hongshen Ma. Microfluidic biomechanical assay for red blood cells parasitized by plasmodium falciparum. *Lab on a Chip*, 12(6):1143–1150, 2012.
- [106] Thurston Herricks, Meher Antia, and Pradipsinh K Rathod. Deformability limits of plasmodium falciparum-infected red blood cells. *Cellular microbiology*, 11(9):1340–1353, 2009.
- [107] Marie-Claire Bélanger and Yves Marois. Hemocompatibility, biocompatibility, inflammatory and in vivo studies of primary reference materials low-density polyethylene and polydimethylsiloxane: A review. *Journal of biomedical materials research*, 58(5):467–477, 2001.
- [108] David T Eddington, John P Puccinelli, and David J Beebe. Thermal aging and reduced hydrophobic recovery of polydimethylsiloxane. *Sensors and Actuators B: Chemical*, 114(1):170–172, 2006.
- [109] Hongbin Zhang and Mu Chiao. Anti-fouling coatings of poly (dimethylsiloxane) devices for biological and biomedical applications. *Journal of medical and biological engineering*, 35(2):143–155, 2015.
- [110] Lydia Mata-Cantero, Maria J Lafuente, Laura Sanz, and Manuel S Rodriguez. Magnetic isolation of plasmodium falciparum schizonts irbcs to generate a high parasitaemia and synchronized in vitro culture. *Malaria journal*, 13(1):1, 2014.

- [111] LE Göran Eriksson. On the shape of human red blood cells interacting with flat artificial surfaces—the ‘glass effect’. *Biochimica et Biophysica Acta (BBA)-General Subjects*, 1036(3):193–201, 1990.
- [112] LB Leverett, JD Hellums, CP Alfrey, and EC Lynch. Red blood cell damage by shear stress. *Biophysical journal*, 12(3):257, 1972.
- [113] Kevin Loutherbach, Kevin S Chou, Jonathan Newman, Jason Puchalla, Robert H Austin, and James C Sturm. Improved performance of deterministic lateral displacement arrays with triangular posts. *Microfluidics and nanofluidics*, 9(6):1143–1149, 2010.
- [114] Ewan Henry, Stefan H Holm, Zunmin Zhang, Jason P Beech, Jonas O Tegenfeldt, Dmitry A Fedosov, and Gerhard Gompper. Sorting cells by their dynamical properties. *Scientific Reports*, 6, 2016.